Chapter 3

Inhomogeneous Elasticity and Viscoelasticity: Effects on Stress-transmission in Ice Streams

As demonstrated in the previous chapter, the geometry of a homogeneous elastic ice stream imposes a stringent restriction on the distance that ocean tidal loads can be transmitted inland of the grounding line. However, ice streams are not uniform elastic bodies. There are bulk material inhomogeneities due to enhanced shear in the marginal ice and vertical temperature gradients in the ice. Additionally, ice deforms viscously over long timescales and preferential flow directions due to ice's polycrystalline nature can align, resulting in anistropic deformation. In this chapter, we first consider the effect of elastic inhomogeneity on the length-scale of the transmission of tidal stresses inland of the grounding line—specifically investigating an increase in the compliance of the ice stream's lateral margins. Increasing the marginal compliance reduces the stress supported by the ice stream's sidewalls, resulting in an increase in the length-scale of stress-transmission. We then explore the role of viscoelasticity in the deformation of the ice stream, in order to quantify the effect that viscoelasticity has on the inferred transmission length-scale of a tidal stress. While we find that viscoelasticity plays an important role in determining the time delay between the peak tidal signal and peak surface motion of the grounded ice stream, the effect on the stress-transmission length-scale is too minor to explain the long-distance observations from Bindschadler and Rutford Ice Streams. Ultimately, we conclude that lacking a mechanism which essentially decouples an ice stream from its lateral margins, a process outside of the bulk

of the ice stream must be responsible for the large zone of tidal influence observed on some Antarctic ice streams.

3.1 Introduction

As alluded to at the end of chapter 2, representing ice as a homogeneous elastic body is not the most realistic rheological model for ice. The choice of material model will directly affect the stress-transmission behavior in our ice stream models. As the calculated stress-transmission length-scales in our three-dimensional ice stream models are too short to match the observations from Rutford and Bindschadler Ice Streams (Gudmundsson, 2007; 2008; 2011; Anandakrishnan et al., 2003), for a realistic rheological change to be significant, the new rheology must weaken the resistance of the ice stream's lateral margins. In this introductory section, we first describe several common inhomogenities in ice's elastic behavior before introducing the range of viscoelastic constitutive laws used in glaciology to model ice deformation. We consider inhomogeneity in elasticity created by the large-scale crevassing of an ice stream's shear margins and what effect such marginal weakening has on the ice stream's ability to transmit tidal loads. We also consider the impact of incorporating a viscous component of ice deformation over the tidal timescales has on the extent of tidally induced deformation of an ice stream. Given the independence of these two rheological considerations we discuss each separately. This chapter closes with a discussion of both elastic and viscoelastic homogeneity as related to field observations from Antarctica.

3.1.1 Elastic Rheological Effects

The impacts of temperature, crystal fabric, and ice purity on the viscous deformation of ice are better constrained than their potential to modify the effective elastic moduli of ice.

While there is no reason to believe *a priori* that the same processes that alter viscous flow of ice will also alter the elastic response of ice, investigating these processes that influence ice viscosity does provide a touchstone for understanding the physical mechanisms behind potential elastic inhomogeneity. For viscous flow, we focus on how three different processes impact the viscosity parameters: temperature-dependent viscosity, fabric-induced preferential viscous flow directions, and enhanced shear in ice stream margins. For each process, we first summarize that process's ability to perturb viscosity of ice then discuss that process's potential to change the (elastic) compliance of ice.

3.1.1.1 Temperature-Dependent Rheology

The West Antarctic ice sheet and ice streams are polythermal glaciers, with temperatures ranging from the pressure melting point to as low as -50 °C (e.g., Gow et al., 1968; Engelhardt, 2004a, 2004b; Salamatin et al., 2008). A bevy of field observations (e.g., Nye, 1953; Jezek et al., 1985, MacAyeal et al., 1996, 1998) and laboratory experiments (e.g., Budd and Jacka, 1989) show a clear temperature dependence in the viscosity coefficient of ice. Following Cuffey and Paterson (2011), the temperature dependence of ice viscosity can be summarized by two different Arrhenius relationships: one for temperatures between 0 and -10 °C, and the other for temperatures colder than -10 °C. For reference, the viscosity coefficient, the nonlinear analog to viscosity, changes by about a factor of 10 between 0 and -10 °C. The large change in the magnitude of ice's viscous deformation with temperature implies that the viscosity coefficient in ice streams can be substantially varied as a function of ice stream depth.

Jellinek and Brill (1956) find that the Young's modulus of ice varies by about 40% over a temperature range of -5 to -15 °C, though there is a large amount of variability in measured moduli. The temperature dependence of elasticity is quite a bit smaller than that of viscosity for a given temperature profile. As a demonstration of how negligible the temperature dependence of ice elasticity is, Jellinek and Brill construct a well-fit rheological model for ice using data from their creep relaxation experiments where only the viscous deformation of the ice is temperature dependent. Of course, if the ice is heated to the point of melting, then the elastic strength of the ice will necessarily plummet; however, for our purposes we will assume that melting is negligible.

3.1.1.2 Fabric Dependence

Glacial ice, being polycrystalline, is known to be strongly anisotropic once creep establishes a preferred crystal orientation. The direction of ice motion relative to the preferred crystalline glide direction dictates the deviation in observed strain rate from that of isotropic ice. The anisotropy of a mature crystal fabric in ice can enhance the strain rate of ice in a "weak" orientation by up to 100 times that of ice in a "strong" orientation (Shoji and Langway; 1988).

Such polycrystalline anisotropy also influences the elastic behavior of ice, as demonstrated through the measurement of seismic anisotropy in glacial ice by Blankenship and Bentley (1987). They found that the variation in seismic P-wave speed in glacial ice is about 10%. This change in wave speed corresponds to a variation in elastic moduli on the order of 20%. Focusing on the slower-moving ice stream, Blankenship and Bentley suggested that a preferentially oriented ice fabric is the cause of the observed change in wave speed. The faster-moving ice stream could conceivably

develop a stronger fabric that could result in an increased influence on the elasticity of ice.

Laboratory results for anisotropy in the Young's moduli of sea ice found a peak to peak variation between 10% and 41%, depending on the nature of the columnar crystallization (Nanthikesan and Sunder; 1995 and references therein). While such laboratory results are not strictly usable to determine the behavior of glacial ice due to the presence of salt in the sea ice's crystalline structure, all the studies presented here suggest that the variation in elastic moduli for polycrystalline ice, with a preferred crystal orientation relative to isotropic ice, is less than a factor of two.

3.1.1.3 Enhanced Deformation in the Shear Margins

In some cases, a single Glen-style viscous flow law is unable to explain observed viscous flow velocities in glaciers over long timescales. Examples include the depth-variable age of ice in ice caps (Paterson, 1991), basal impurities in mountain glaciers (Dahl-Jensen and Gundestrup, 1987; Echelmeyer and Wang, 1987), and most importantly the highly strained ice in the shear margins of West Antarctic ice streams (Echelmeyer et al., 1994). These studies adopted an *ad hoc* spatially variable viscous enhancement factor to the strain rate, effectively reducing the viscosity in regions where the researchers observed rapid velocities.

For the case of ice stream shear margins, this viscous enhancement can be as large as a factor of twelve. In Echelmeyer et al.'s (1994) study of Whillans Ice Stream, the regions of viscous enhancement correspond to a "chaotic zone" of intense, irregular crevassing. While these researchers did not physically model the interaction between the crevasses and the viscous flow of the ice stream, they point to the crevassing as an

indication of high shear strain, suggesting that a strain-weakening process (such as shear heating, their preferred hypothesis) could be the cause of the necessary enhancement to ice velocity. Such an approach is equivalent to increasing the effective ice stream width.

As discussed earlier, the temperature dependence of ice elasticity is substantially smaller than that of ice viscosity, suggesting that shear heating is not a major player in potentially changing the elasticity of an ice stream's margins. However, the presence of crevasses (or more generally, cracks) within elastic bodies is known to influence the effective elastic moduli of the damaged body. As demonstrated by Walsh (1965) for a penny-shaped crack, a reduction in the magnitude of the Young's modulus of an elastic body can approximate the increased deformation of the body due to the presence of void space or frictional cracks.

The number of crevasses is difficult to accurately quantify as only surface crevasses are directly observable, making any attempt to create a "crevasse distribution" for a given glacier intractable from a remote sensing perspective. Furthermore, small scale cracking in ice can be pervasive, rendering it impossible to calculate an effective rheology from an applied mechanics formulation such as Walsh (1965). The limitations on the measurement of cracks in glacial ice suggests that using an empirical fit of damage parameters estimated from observations is the simplest method of finding the approximate magnitude of the enhancement in ice's elastic response due to damage in the bulk of the ice.

Unfortunately, current measurement of the magnitude of the elastic response of ice streams is limited to GPS stations placed near to short-term perturbations to the background stressing of an ice stream. Of most immediate relevance are the GPS surveys

of the ocean tidal loading of ice streams in Antarctica presented in Chapter 1. However, with the exception of the surveys of Whillans Ice Plain by Winberry et al. (2009; 2011), these GPS surveys lack the spatial coverage to resolve the potential difference in displacement response of the shear margins versus the interior of the ice stream. And, in the case of the Whillans Ice Plain, the stick-slip nature of the GPS data obscures any simple variation in the elastic response between the central and marginal ice. The stick-slip behavior, controlled by poorly understood basal friction properties of the ice plain, would necessarily be convolved with any increased effective compliance in the shear margins due to damage in the margins. As such, we cannot rule out strain-weakening in the shear margins as a potentially important elastic inhomogeneity based on the current suite of field observations alone.

3.1.2 Appropriateness of Viscoelasticity

The analysis of ice motion is traditionally treated as a problem of viscous, rather than elastic, deformation (e.g., Cuffey and Paterson, 2011). While the timescale in the standard ice problem is months and years rather than hours and days, the prevailing large-scale deformation of ice is clearly viscous in nature. As such, we now explore the possibility that the viscous component of deformation in ice streams is important at hourly to weekly timescales in the context of the transmission of tidal loads inland of an ice stream's grounding line.

Recent research suggests that viscoelasticity is necessary to correctly model the tidal behavior of ice streams. Gudmundsson (2007) and King et al. (2011) explicitly state that viscoelastic effects within the ice stream may play a role in the phase delay of the ice stream's response to tidal loading. Gudmundsson (2011) and Walker et al. (2012) carry

out two-dimensional flow-line models with viscoelastic rheologies and find that these models fit observations more satisfactorily than an equivalent elastic ice model. Even though we have demonstrated that flow-line models fail to correctly predict the length-scale of the transmission of tidal stresses, the flow-line models of Gudmundsson and Walker et al. suggest that viscoelasticity can play a role in the transmission of tidal stresses inland of the grounding line of an ice stream.

Additionally, rheological modeling of ice deformation in the laboratory suggests that ice behaves viscoelastically (e.g., Jellinek and Brill, 1956; Goldsby and Kohlstedt, 1997; 2001; Morland, 2009; Riesen et al., 2010). These studies focus on using viscoelastic fluid models to improve the mathematical representation of the three creep regimes of ice (primary, secondary, and tertiary creep). As will be discussed in subsection 3.1.2.1, our choice of a Maxwell viscoelastic material model is a simpler rheology than those suggested by the aforementioned laboratory studies. A Maxwell model captures the behavior most relevant to the tidal perturbation of ice stream flow. Following this discussion, section 3.1.2.2 outlines our expectations for the relative importance of the viscous and elastic deformations in our models at different timescales, using the Maxwell relaxation time as an intuitive metric.

3.1.2.1 Simple Rheological Models for Viscoelasticity

Multiple models for viscoelasticity exist, so we must contemplate the most appropriate model for ice. We consider the three simple viscoelastic material models shown in figure 3.1: the Maxwell, Kelvin-Voigt, and Burgers models. We will choose to implement viscoelasticity in ice as an isotropic Maxwell model, which has the benefit of capturing

the most relevant characteristics of ice deformation while being simple enough to be well constrained using laboratory data.

A Maxwell viscoelastic model is comprised of a spring (elastic) element in series with a dashpot (viscous element). The canonical one-dimensional form of a linear Maxwell element is given as:

$$\dot{\varepsilon} = \frac{\sigma}{\eta} + \frac{\dot{\sigma}}{E} \tag{3.1}$$

A Maxwell material represents a fluid, as a constant stress will converge to a constant strain-rate, and thus linear time-dependent deformation. An advantage of the Maxwell model is that the elastic and viscous responses of the material are easily separable for problems with a characteristic stress as these responses are additive.

In contrast, the Kelvin-Voigt material is comprised of a spring element in parallel with a dashpot element. Equation 3.2 shows the canonical form of a linear Kelvin-Voigt element:

$$\sigma = E\varepsilon + \eta\dot{\varepsilon} \tag{3.2}$$

At its core, the Kelvin-Voigt model is that of a deformable solid, as a constant stress will result in the time-dependent relaxation to a strain value of that of an equivalent elastic model. And opposed to the Maxwell model, the Kelvin-Voigt model is easily separable into elastic and viscous portions for problems with a characteristic strain.

A third common viscoelastic rheology, the four element Burgers model, combines a Maxwell element in series with a Kelvin-Voigt element. The one-dimensional constitutive law is given by:

$$\sigma + \left(\frac{\eta_1}{E_1} + \frac{\eta_1}{E_2} + \frac{\eta_2}{E_2}\right)\dot{\sigma} + \frac{\eta_1\eta_2}{E_1E_2}\ddot{\sigma} = \eta_1\dot{\varepsilon} + \frac{\eta_1\eta_2}{E_2}\ddot{\varepsilon} \tag{3.3}$$

where the subscript 1 corresponds to the Maxwell element and the subscript 2 corresponds to the Kelvin-Voigt element. The defining characteristics of a Burgers model are that there is both an instantaneous and a long-term viscous response controlled by the Maxwell element, but that the transition between these two is smoothed due to the viscous deformation of the Kelvin-Voigt element (see figure 3.2).

Recalling that ice is best represented by a stress dependent viscous term, the gravitational stress driving the flow of the ice stream cannot be separated from the tidal perturbation of the stress field. As this limitation requires that our ice model can flow under its own weight, a fluid model is required, thus ruling out the (solid) Kelvin-Voigt model as an appropriate ice model.

From the published literature, ice is commonly modeled as a four element Burgers body with a nonlinear Maxwell body and a linear Kelvin-Voigt element (e.g., Jellinek and Brill, 1956; Reeh et al., 2003; Gudmundsson, 2007; Tsai et al., 2008). However, we opt to use a Maxwell material for ice in our modeling for two reasons. First, Reeh et al. (2003) demonstrates that the use of the simpler Maxwell rheology to fit tidal flexure data is only slightly worse than the fit using the Burgers rheology. Second, the experimental data of Jellinek and Brill (1956) suggests that the retardation time in the Kelvin-Voigt element is on the order of 10^2 seconds. As our tidal forcing acts on the timescale between 10^4 and 10^6 seconds, the influence of the Kelvin-Voigt element will be negligible compared to the behavior of the Maxwell element (shown in figure 3.2). Figure 3.2 demonstrates that the Maxwell element captures the initial elastic response and the tertiary creep of ice, with only the transitional region being poorly fit. Thus, we use the following nonlinear Maxwell material model for the viscoelasticity of ice:

$$\dot{\varepsilon} = A\sigma^n + \frac{\dot{\sigma}}{E} \tag{3.4}$$

3.1.2.2 The Maxwell Relaxation Time

In a Maxwell viscoelastic model the relative importance of elastic and viscous deformation in the material is quantified by a Maxwell relaxation time, T_{Max}:

$$T_{Max} = \frac{\eta}{E} \tag{3.5}$$

If $T_{Max}$is large, the material will response elastically to an applied load. If T_{Max} is small, then the material's response to an applied load will be viscous in nature. However, tidal loading is not a constant force but rather acts as a time-variable stress. The dimensionless Deborah number, *De*, quantifies the relative importance of the viscous or elastic response to the timescale of the loading function and is given by:

$$De = \frac{T_{Max}}{t_f} \tag{3.6}$$

where t_f is the period of the forcing function. If *De* is small, then the material's response will be primarily viscous; if *De* is large, then the response will be primarily elastic.

Given the stress dependence of the effective viscosity of ice, *De* is inexorably tied to the amplitude of the deviatoric stress in the material, and will vary with the magnitude of the stress field in the material. As such, we define a transitional stress, σ_{trans}, to be where the material's response changes from being primarily viscous to primarily elastic, though in the region of this transitional stress, both components of deformation are important. σ_{trans} is defined as:

$$\sigma_{trans} = \left(AEt_f\right)^{-\frac{1}{n}} \tag{3.7}$$

Stresses higher than σ_{trans} denote a viscously dominated response, while an elastic response dominates when the stresses fall below σ_{trans}. As the frequencies of the tidal components vary, there are separate transitional stress levels for the semi-diurnal, diurnal, and fortnightly tides. Table 3.1 summarizes the expected transitional stresses using a value of A for T=0°C through T=-25°C and a value of $n=3$ (Cuffey and Paterson, 2011). σ_{trans} varies between a few and a few hundred kPa, which is the same order of magnitude as background driving stresses and the tidal stresses in our ice stream models. Thus, we expect there to be an even partitioning of stress and deformation between ice's elasticity and viscosity. The ice's response is unlikely to be well approximated by either a purely elastic or a purely viscous model. Reducing Young's modulus (while holding the viscosity coefficient fixed) increases the transitional stress to a viscously dominated response. Thus, invoking damage as a mechanism to increase the compliance in the ice margins may reduce the effective stress support of the margins in an elastic model. However, such a damage model implies that the viscoelastic response of the ice margins will be less pronounced than that of the central ice unless the effective viscosity of the lateral margins is reduced along with the Young's modulus.

3.2 Strain-Weakening in the Shear Margins

From the previous discussion, only damage in the shear margins provides the potential for large-scale elastic decoupling of an ice stream from its lateral margins. We begin with a continuum damage mechanics formulation to provide some physical basis for introducing an inhomogeneous Young's modulus into our three-dimensional elastic models from chapter 2. We investigate two different profiles for spatial variations in elasticity. We then discuss the implications of increasing compliance in the shear

margins, comparing our results to observations of both tidal stress-transmission and damage estimates from Antarctica.

3.2.1 Continuum Damage Mechanics Formulation

As the theoretical and observational constraints suggest that the variability of ice stream elasticity with the temperature and fabric is limited to a factor of two at best, we focus solely on the effect of strain-weakening on the elastic moduli of ice. To model the impact of individual crevasses is intractable due to the lack of a complete understanding of crevasse formation and distribution (e.g., Cuffey and Paterson, 2011), and the computational burden such a model would require when considering an ensemble of crevasses. However, the finite element formulation allows for spatially variable material parameters. Implementing a continuum damage mechanics approximation of the damage due to crevassing potentially allows our models to connect crevassing with the effective material moduli of the ice, without needing to explicitly model individual fractures.

To parameterize damage, we consider a parameter *D* such that

$$\dot{\varepsilon} = A\left(\frac{\sigma}{1-D}\right)^n \tag{3.8}$$

is the modification of the viscous (Glen) flow law due to the presence of damage in the given viscous element of the model. This formulation is equivalent to following *Kachnov-Rabotonov theory* (Kachanov, 1958, 1986; Rabotnov, 1968) with no evolution of *D*, a fair assumption over the short timescales in our problem. The damage parameter *D* can take a value between 0 (no damage) to 1 (complete plastic failure of element), and can be interpreted of a fraction of volume in the problem that can no longer support a load due to the opening of void space in the damaged body (see figure 3.3). This linear

damage mechanics formulation breaks down at large damages (*D>~0.90*), where a real body would lose coherence. However, for small to moderate damages, a linear damage mechanics formulation provides a physical connection between fracture and a reduction in effective material parameters.

For the modification of elastic moduli, this form of continuum damage maps directly into the linear elastic constitutive equation (Chaboche 1977; Lemaitre and Chaboche, 1978) as:

$$\varepsilon = \left(\frac{\sigma}{E(1-D)}\right) \tag{3.9}$$

If the two rheological models are connected as a Maxwell viscoelastic material, it follows directly from conservation of effective stress that the rheological model with damage looks similar to equations 3.8 and 3.9, except that the viscous response D_1 may be different from the elastic response D_2

$$\dot{\varepsilon} = A\left(\frac{\sigma}{1-D_1}\right)^n + \left(\frac{\dot{\sigma}}{E(1-D_2)}\right) \tag{3.10}$$

The above equation only holds if the values of *D* are held constant through time. Figure 3.3 shows a schematic for such a viscoelastic damage formulation. For the analysis in this chapter, we will only consider equation 3.9 (linear elasticity with damage).

A critical piece of information is the value of *D* that approximates the expected damage within an ice stream's shear margin. We begin by making the assumption that $D_1 = D_2 = D$ as there are neither laboratory nor observational constraints on the effects of damage on ice elasticity. The results from Echelmeyer et al.'s (1994) study on the viscous enhancement of ice stream flow are used to approximate the viscous *D*.

Following the derivation of Borstad et al. (2012), the relationship between *D* and the enhancement factor *En* of Echelmeyer et al. is:

$$En = (1 - D)^{-n} \tag{3.11}$$

Using the peak enhancement factor of 12 from Echelmeyer et al. and the canonical *n=3* gives *D=0.56*, which corresponds to a reduction in Young's modulus by about a factor of two. Given our uncertainty in the relationship between the *D* values of viscous and elastic ice, we extend our search to include values of *D* that change the Young's modulus by up to three orders of magnitude. Albeit unphysical, this broad selection of values allows us to empirically derive a robust relationship between *D* and L_{tr}. Based on estimates of damage necessary for crevassing, discussed in more detail later, we expect that the physical range of values for *D* are between 0.0 and about 0.6 (e.g., Borstad et al., 2011).

We must still decide how to distribute damage throughout an ice stream. We begin with models that have a linearly varying value of *D=0* at the margins to a predetermined *D* at the edge of the ice stream ("continuous margins"). We use these models to explore a large range of effective Young's modulus values in order to characterize the relationship between the length-scale for transmission of stress L_{tr} and the relative magnitude of the reduction of Young's modulus in the margins (as discussed in section 3.2.2). We then move to models where there is a step-function transition from *D=0* to *D≠0* at a predetermined shear margin boundary ("discrete margins"). Such models explore the importance of the size of a shear margin on the value of L_{tr} using a pattern of *D* meant to approximate that seen viscously in ice streams (see section 3.2.3). Figure 3.4 shows sample profiles for both types of models.

3.2.2 Continuous Margin Results

Figure 3.3 shows a representative stress state from a model with a linear variation in Young's modulus of one order of magnitude between the compliant margins and the more rigid central ice. While the stress state is similar to that of the homogeneous elasticity model in figure 2.6, there are important differences when the elasticity is inhomogeneous. First, L_{tr} is longer throughout the model with the compliant margin than in the homogeneous model. In this specific model, the length-scale for the transmission of stress is about 1.6 times longer than that of a homogeneous model. Note that the value of L_{tr} is constant across the profile of the model ice stream (save immediately near the grounding line), even though the Young's modulus is not. Second, the continuous margin model concentrates stress at the center of the ice stream, as is apparent most readily in the longitudinal normal stress component. In this stress component, the stress is almost an order of magnitude higher in the central regions of the ice stream with the inhomogeneous elasticity than with the homogeneous Young's modulus. The potential for concentration of stress in the central portion of the ice is another example of a three-dimensional effect that simple flow-line models miss.

We considered twelve models with varying values of E at the lateral margins and central ice, ranging from ice 1000 times more compliant in the center to ice 1000 times more rigid in the center. For each of these models, figure 3.6 shows the trend of the change in L_{tr} compared to the homogeneous model as a function of the ratio of E between the central and marginal ice. Thus, as marginal ice is made progressively more compliant, an applied load will decay over longer distances. The converse is also true for situations where the marginal ice is more rigid than the central ice. Finally, the power

law form of the relationship between L_{tr} and E implied an effect for increasing the compliance of the margins. Over the range of models investigated here, the maximum increase in L_{tr} is a factor of about 4.2 when the margins are 1000 times more compliant than the central ice. The change to L_{tr} depends not on the absolute values for E in the model, but rather only on the ratio of E_H and E_L.

3.2.3 Discrete Margin Results

Figure 3.7 shows a representative distribution of the six stress components for a model with discrete ice margins chosen to be one quarter of the ice stream width. When compared to the homogeneous elastic model in figure 2.6, the stress state in the inhomogeneous model looks similar in general pattern to the homogeneous model, but there is a noticeable perturbation in stress state near the transition between compliant margins and rigid central ice. In the inhomogeneous model, stress is concentrated in either the central ice (longitudinal normal stress, σ_{xx}) or the margins (the other five components). Unlike the continuous margins models, L_{tr} is not constant across a transverse profile of the ice stream. Additionally, values for L_{tr} in these discrete margin models are larger than that of the homogeneous elastic models, just as was seen earlier in the continuous margins models.

To quantify the increase in L_{tr} due to the presence of compliant margins, we consider the vertically-averaged value of L_{tr} derived from the equivalent stress, rather than component by component. Figure 3.8 illustrates the behavior of different margin widths and L_{tr} for two models with discrete margins one order of magnitude more compliant ($E_H/E_L=10$) than that the central ice. The first panel (A) shows the results for an ice stream 10 kilometers wide and 1 kilometer thick, while the second panel (B) shows

the results for an ice stream 20 kilometers wide but otherwise identical. Consider first the left-hand plots, which show the transmission length-scales for eleven models that have discrete margins making up from 0% to 100% of the ice stream width at intervals of 10%. Circles represent the locations of the transition between the marginal and central ice. We note three features:

1) The values of L_{tr} are identical for models with 0% and 100% compliant margin widths. This result is expected as these models equivalent to uniform elasticity.

2) The variation of L_{tr} across the ice stream's profile (i.e., in the x-direction) is strongly dependent on the model parameters, such as the relative size of the margins and the absolute width of the ice stream. Take, for example, the 50% margin width and the 80% margin width profiles in panel A. In the former, L_{tr} peaks in the marginal ice near the transition between the two rheologies and is slightly decreased in the central ice. In the latter, L_{tr} in the central ice is elevated compared to that of the margins. Further, note that the profiles of L_{tr} between the two models are different.

3) The largest value of L_{tr} occurs in the models that have margins that make up 50% of the ice stream half-width or 25% of the ice stream full-width. As an aside, we note that this margin width is similar to the best-fit marginal width found by Echelmeyer and others (1994) for viscous flow models of Kamb Ice Stream. More work is necessary to determine if the similarity in peak margin width between elastic and viscous

models is coincidental or if this result suggests that our assumption that $D_1=D_2=D$ is permissible.

4) The discontinuities in the profiles of L_{tr} are due to the use of the equivalent stress to define the transmission length-scale. This jump in L_{tr} is caused by: one, the equivalent stress depends on the longitudinal stress (σ_{xx}); two, the longitudinal stress can be discontinuous across the jump in Young's modulus. The displacements are continuous across the discontinuities in Young's modulus.

The right-hand plots in figure 3.8 demonstrate the relationship between margin size and L_{tr} for a tidal forcing. These plots show the average value of the L_{tr} (with error bars indicating 1 standard error of the mean) as a function of relative margin width. As mentioned earlier, we find that the maximum increase in L_{tr} relative to the homogeneous elastic model occurs when the shear margins are one quarter of the ice stream width. However, due to the polynomial form of L_{tr} as a function of margin width, even a fairly small shear margin can increase L_{tr} by a factor of 2 to 3. Additionally, the average value of L_{tr} shows only a minor dependence on the geometry of the ice stream, as demonstrated by the small difference in maximum value of L_{tr} between 10 and 20 kilometer wide models.

3.2.4 Strain-Weakening Discussion

The results of our models incorporating inhomogeneous elasticity in the shear margins demonstrate that the nature and variability of ice's elastic moduli within the ice stream can have a profound effect on the transmission of a tidal load inland of the grounding line. This connection between elastic moduli and stress-transmission exists even though

the transmission of stress in homogeneous elastic models is independent of the elastic moduli. Thus, if the elastic moduli of ice vary across an ice stream, it is not sufficient to calculate effective elastic moduli for the entire ice stream as this cannot correctly model the stress-transmission.

While the relative increase in L_{tr} in our models is only between 1 and 3 times the value of L_{tr} in our homogeneous models for values of strain-weakening D that match those seen viscously, this variability represents a difference in many tens of kilometers of stress-transmission—the very length-scale of tidal stress-transmission seen geodetically. To our knowledge, there currently are no observations of *in situ* ice elasticity that suggest there is a reduction in Young's modulus within the shear margins of ice streams. However, simple models of ice fracture and crevassing suggest that an ice stream's shear margins should be more compliant than the (relatively) undamaged central portions of the ice stream.

As independent constraints on the variability of elasticity do not exist, our results from these inhomogeneous finite element models define the range of potential parameter space necessary to explain the observed tidal signal from the GPS stations on Rutford and Bindschadler Ice Streams, rather than test specific values. Referring back the values of L_{tr} found in section 2.4 for the homogeneous elastic models, figure 3.9 shows that an increase in the range of 2.67 (fortnightly tide) to 3.32 (semidiurnal tide) for Rutford Ice Stream and about 4.40 (semidiurnal tide) for Bindschadler Ice Stream from the homogeneous elastic stress decay length would be close enough to explain the amplitudes of displacement seen in the GPS records.

We can create an empirical margin-width dependence from our 20-kilometer-wide model, fitting the model results shown in figure 3.8B. We fit the model results using a polynomial fit of degree four as this is the lowest degree polynomial that falls within one standard error of the mean for the average stress decay length increase values. We also impose the added constraints that the end points must have a value of relative $\hat{L}_{tr}$ equal to 1 as our shear margin results must necessarily converge to the homogeneous elastic solution when there is no variation in elastic moduli.

We now use the marginal-compliance relationship from figure 3.6 to define the dependence of changes in L_{tr} on the relative value of E in the compliant margins. We use these two fits to create a map in margin-width vs. compliance space that allows for the model to match the observations (figure 3.9). Figure 3.9 shows the range of margin-widths and reductions in Young's modulus necessary to increase the overall value of L_{tr} by certain amounts. Not surprisingly, the maximum increase to L_{tr} occurs when the shear margins are about 50% of the ice stream half-width (25% of the ice stream full-width), and when the lateral margins are substantially more compliant than the central ice stream. This plot also shows the three lines in margin size-compliance ratio space that would be sufficient to match the values of L_{tr} found for compliant margins models approximating Bindschadler and Rutford Ice Streams to the observations of the decay of tidally induced displacements. In these cases, the minimum values of D are found to be: 0.988 for the fortnightly Rutford tide, 0.996 for the semidiurnal Rutford tide, and 0.999 for the semidiurnal Bindschadler tide.

To add some physical meaning to these estimates of D, we compare these modeled values to the critical damage threshold values of D, commonly named D_C, found

in the literature. From laboratory experiments, D_C has been approximated from between 0.45-0.56 for ice (Pralong and Funk, 2005; Duddu and Waisman, 2012). From analysis and numerical inverse modeling of a continuum damage mechanical viscous model of the Larsen B Ice Shelf collapse, Borstad et al. (2012) found the value of D_C for calving to be 0.6±0.1. To compare D_C with our model results, we must remember that the above values for D_C are for nonlinear viscous flow, such that the "enhancement" value is governed by equation 3.11. Thus, the corresponding enhancements are between about 6 (for 0.45) and 37 (for 0.7) using the canonical power law exponent for Glen flow of $n=3$. Unfortunately, even our smallest necessary enhancement has a value of 467.7 ($10^{2.67}$, for the fortnightly tide on Rutford Ice Stream), strongly suggesting that the necessary damage to have marginal compliance be the sole explanation of our models and observations is too high to be physically reasonable. The situation is exacerbated for other tidal periods, with the necessary enhancement being factors of ~2,000 and ~25,000. Thus, marginal compliance alone is insufficient to bring our modeled stress decay length-scales into line with those found observationally from GPS stations on the Rutford and Bindschadler Ice Streams.

3.3 Viscoelasticity

As strain-weakening of the shear margins does not explain the difference between our modeling results and the long-distance stress-transmission observed on some Antarctic ice streams, we now investigate the potential for viscoelasticity to decouple the ice stream from its lateral margins and thus increase the transmission length-scale of a tidal load. Section 3.3 begins with a discussion of the modeling considerations necessary in a nonlinear viscoelastic model that are otherwise not present in a linear elastic finite

element model. We then present results from two types of viscoelastic models: one set with a homogeneous viscosity coefficient (section 3.3.2) and another with a temperature-dependent viscosity coefficient (section 3.3.3). The final portion of this section relates our viscoelastic modeling to the observed stress-transmission length-scales from Antarctica.

3.3.1 Viscoelastic Model Considerations

Incorporating both viscoelasticity and nonlinearity into our constitutive law for ice introduces many additional modeling concerns in order to correctly study the link between ocean tides and ice stream motion. The first change is that our model has stress-dependent viscosity, and thus stresses within the ice stream other than the tidal loading can no longer be neglected, as was done for the linear elastic models. Also, as viscous deformation is a time-dependent process, our viscoelastic models must explicitly account for the time-variability of our tidal loading condition. We address both of these issues in turn.

3.3.1.1 Nonlinearity and the Loss of Superposition

In our linear elastic models, the principle of linear superposition allowed us to isolate tidally induced deformation from the background driving stresses in our models. With the change to a nonlinear viscoelastic rheology, we must now consider the stress state of our model ice stream more carefully as we cannot simply neglect the non-tidal stresses when designing our models. As the ice's viscosity depends on the total deviatoric stress throughout the ice stream, the effective viscosity of the ice stream will be both spatially and temporally variable. The total deviatoric stress necessarily includes the tidal and non-tidal deviatoric stresses. To correctly account for the "true" value of viscosity, our

models must now incorporate the deviatoric component of the gravitationally-derived driving stress and the extensional stress balance at the interface between the ice stream end and the ocean.

(1) Driving Stress in the Ice Stream

All glaciers, by definition, flow under their own weights, as discussed earlier in section 1.4. As a reminder, the shear (deviatoric) stress induced in the direction of flow is commonly taken as (e.g., Cuffey and Paterson, 2011):

$$\tau_b = \rho g H \sin\alpha \tag{3.12}$$

where α is the surface slope of the glacier. The basal slope of the glacier is, to first order, not important in determining the basal shear stress.

Very shallow surface slopes, and thus low basal shear stress values, are characteristic of the Antarctic ice streams with long-distance stress-transmission. Using estimates of ice stream basal stress from ice streams on the Siple Coast (~ 100 kPa, Cuffey and Paterson, 2011), we estimate a reasonable surface slope of about 0.57 degrees. While a stress of 100 kPa is small when compared to the hydrostatic pressure at the base of these ice sheets (which can be upwards of 10 MPa), this driving stress is still larger than the stress change due to a one meter oceanic tide. Furthermore, this deviatoric stress value suggests that ice is about ten orders of magnitude more viscous at the ice stream's base than at the surface due to the stress dependence of the effective viscosity!

For our models, we apply only the downhill (i.e., deviatoric) portion of the gravitational driving stress. Figure 3.10 shows our approach schematically. The modeled ice stream is assumed to have a constant surface slope of α and thickness H, such that our deviatoric gravitational vector is at an angle α to the model's horizontal

coordinate axis. This modeling approach is a permissible simplification of an ice stream's geometry as the basal slope does not strongly affect the induced shear stress at the base and the shallow surface slope means that the ice stream's thickness would not change dramatically over the length-scale of the tidal stress-transmission. In the finite element formulation, we apply the horizontal component of gravity, with a magnitude of $g_{horiz} = g \sin \alpha$, to our model as a time-constant acceleration acting on the entire ice body.

Neglecting the non-deviatoric component of gravity is convenient as the model viscosity is independent of the hydrostatic stress and additionally removes the need to apply a pre-stress to cancel out the compression due to "turning on" gravity at the initial timestep. However, at the ends of the ice stream, the hydrostatic pressure for real ice streams is not balanced completely by the ocean tide. The excess hydrostatic pressure acts as a force that "pulls" the ice stream in the direction of flow, which causes a deviatoric extensional stress on the edge of the ice stream (Cuffey and Paterson, 2011). We discuss this extensional stress next.

(2) Ocean-Ice Interface

At the downstream edge of an ice stream, the hydrostatic pressure due to a glacier's weight is resisted primarily by the hydrostatic force of the ocean acting on the ice shelf. Due to the dependence of the effective viscosity on the deviatoric stress, any mismatch in hydrostatic pressures between the ice stream and the ocean will result in a deviatoric stress that reduces the ice stream's viscosity near the grounding line. This deviatoric stress is independent of any flexural stresses caused by a rising and falling ice shelf.

In Appendix 3A, we consider the effects of these stresses on the viscoelasticity deformation of an ice stream. There we show that any extensional or flexural stresses do not perturb the effective viscosity near the grounding line enough to cause significant variation in our model results from those following the much simpler tidal condition used in the elastic models. Therefore, we model the ocean tidal perturbation in ice stream velocity as an oscillatory normal stress acting at the ice stream's grounding line—the same configuration as in our linear elastic models.

3.3.1.2 Time-Dependent Behavior

Deformation of a viscoelastic (or more generally, viscous) material will inherently be time-dependent. Thus, our models must accurately resolve the time-dependent behavior our ice stream system. Time-dependence enters our problem in two ways: the time-varying nature of the forcing function, and the time-dependence of ice stream's tidal response.

(1) Time-Dependent Loading

Oscillations of the ocean tides represent a time-dependent force on an ice stream. While there are numerous tidal frequencies, we focus on the three largest tidal constituents acting on ice streams: the semidiurnal, diurnal, and fortnightly tides. The GPS surveys of Anandakrishnan et al. (2003), Gudmundsson (2007; 2008; 2011), and Winberry et al. (2009; 2011) all use the GPS vertical deformation of a station placed on the (floating) ice shelf as a measurement of the ocean tides. The observed ocean tidal amplitude displays a strong beat frequency (see figure 3.11). To approximate the amplitude of the tidal component, we select the two largest semidiurnal and diurnal components, along with the fortnightly tide, from the FES2004 tidal model (Lyard et al., 2006) to create a synthetic

tidal signal. The tidal data is then fit using a nonlinear least squares algorithm to find the amplitude and phase of these five tidal components in the data from the Ross and Weddell Seas (data courtesy of S. Anandakrishnan and H. Gudmundsson). For reference, the Ross Sea abuts the ice streams of the Siple Coast, while Rutford Ice Stream flows into the Weddell Sea. Table 3.2 summarizes the tidal amplitudes and phases from FES2004 and the observational fits, while figure 3.11 shows the real and synthetic tides for the Ross and Weddell Seas.

The agreement between the tidal model and the observations is not strong, with only the semidiurnal and diurnal components in the Weddell Sea coming close to matching. As the point of this section is not to analyze the difference between tidal data and tidal models but rather to approximate the tidal amplitudes for our model ice stream, we choose to use the floating ice GPS stations for constraining the tidal forcing function. These data demonstrate that:

1) The semidiurnal tide is stronger (i.e., larger amplitude) than the diurnal tide which in turn is stronger than the fortnightly tide in the Weddell Sea results, but not in the Ross Sea results.
2) The fortnightly tide, while not always of the smallest amplitude, is subordinate to the either the semidiurnal or diurnal tide, depending on which is the dominant tidal amplitude.
3) The maximum tidal amplitude has a one to two meter amplitude in the two major Antarctic seas. While amplitudes may be larger locally (e.g., Gudmundsson, 2007), we will use a one meter tide as our characteristic amplitude.

We use three tidal constituents (i.e., the semidiurnal tide, the diurnal tide, the fortnightly tide) as forcing functions in our nonlinear viscoelastic finite element models. For simplicity, we approximate the tidal periods of these tidal constituents as 12 hours, 24 hours, and 14 days, respectively. As a reminder, the three tidal constituents cannot strictly be separated due to the nonlinearity in this viscous deformation. However, modeling the response of our ice stream model to a single tidal component is more straightforward and provides an estimate of the expected change in stress-transmission as a function of the tidal forcing period.

(2) Time-Dependent Stress and Displacement Fields

A viscoelastic medium will experience a phase delay between an applied oscillatory load and the deformation response. In the context of ice streams under tidal forcing, this phase delay is expressed as a time-lag in the peak stress and displacement perturbation of the ice stream. In the GPS observations of Rutford Ice Stream (Gudmundsson 2007, 2008, 2011), a phase shift is both observed and seen to vary with distance inland of the grounding line.

In our models, we need to differentiate between the effects of the oscillatory loading of the ocean tides and those of the static loading due to the gravitational driving stress in the ice stream. To this end, we run models both with and without the oscillatory component of the tide. We then subtract the non-oscillatory results from the tidally-forced models. Due to the nonlinear viscoelasticity, the resulting stress field is not strictly the ice stream's response to the oscillatory loading, but rather the change in ice stream response due to the addition of the time-variable component of the tide. As the oscillatory load is several orders smaller than the static loads for most ice streams, we

expect that the response to the variation in total deviatoric stress due to the tides will be approximately linear, and thus the above approach provides results that are close to the ice stream's response to the ocean tides alone.

3.3.1.3 Temperature-Dependent Viscosity

As mentioned in section 3.1.1, the viscosity of ice is strongly temperature dependent (e.g., Cuffey and Paterson, 2011; and references therein), with ice having reduced viscosity at higher temperatures. Numerous laboratory experiments and field observations show that this temperature dependence takes the form of an Arrhenius relationship in the viscosity coefficient *A*, with two distinct regimes depending on the proximity of the ice temperature to the pressure melting point of ice (Weertman, 1983; Hooke and Hanson, 1986; Paterson, 1994). The temperature dependence of the viscosity coefficient, from Cuffey and Paterson (2011), is:

$$A = 3.5 * 10^{-25} \exp\left(\frac{-6 * 10^4}{8.314} * \left[\frac{1}{T} - \frac{1}{263}\right]\right) Pa^{-3} s^{-1}$$

$$\text{for } T < 263\ K$$

$$A = 3.5 * 10^{-25} \exp\left(\frac{-1.39 * 10^5}{8.314} * \left[\frac{1}{T} - \frac{1}{263}\right]\right) Pa^{-3} s^{-1} \tag{3.13}$$

$$\text{for } T > 263\ K$$

where *T* is measured in Kelvins.

Antarctic ice streams have been observed to have a strong temperature gradient from base to surface (e.g., Engelhardt et al., 1990; Engelhardt and Kamb, 1993; 1998; Engelhardt 2004a/b), with some ice stream beds being up to twenty degrees Kelvin warmer than the ice stream's surface. This temperature range corresponds to a variation in the viscosity coefficient by almost a factor of 60. Therefore, we impose a temperature

gradient in our models and use a temperature-dependent viscosity. We adopt an empirical fit of temperature data from Whillans Ice Stream as the temperature profile in all our models. The temperature gradient of such a temperature profile is defined by Engelhardt and Kamb (1993) as:

$$\frac{dT}{dz} = q_b e^{-y^2} + \frac{\lambda a u l}{\kappa} e^{-y^2} \int_0^y e^{-t^2} dt \qquad (3.14)$$

where $= z/l, l = 2\kappa H/a$, q_b is the basal temperature gradient, a is the accumulation rate, u is the ice stream horizontal velocity, κ is the thermal diffusivity, H is the ice stream thickness, and λ is the temperature gradient in air. All values of these parameters, save for model geometries, are taken from Engelhardt and Kamb (1993). In solving for the temperature profile, we set the basal temperature equal to the pressure melting point of ice, -0.7 °C. The results based on a homogeneous temperature field are discussed in section 3.3.2., while the temperature-dependent results are discussed in section 3.3.3

3.3.1.4 Enhanced Flow in the Margins

Observations suggest that enhanced viscous flow exists in the shear margins of ice streams, with the enhanced viscous deformation in the marginal ice being up to twelve times that expected for models using homogeneous laboratory values of ice viscosity (e.g., Dahl-Jensen and Gundestrup, 1987; Echelmeyer and Wang, 1987; Paterson, 1991; Echelmeyer et al., 1994). From equations 3.9 through 3.11, we expect that marginal ice would need a reduction to the value of the nonlinear viscosity coefficient by a value of about 0.56 to produce such an enhanced flow. As increasing the elastic compliance of the margins of a model ice stream resulted in an increase in the distance a tidal load can be transmitted inland of the grounding line, we expect that a reduction in viscosity would produce a similar increase in the stress-transmission length-scale.

However, we do not specifically model possible enhancement in both the elastic and viscous deformation of the shear margins in this thesis. The relative influence of damage on the elastic and viscous deformation is not known, making any assumption about the interaction of *D* and *En* difficult to justify. For example, if *D* is assumed to be constant between the viscous and elastic enhancement, then the viscosity would decreased by $(1-D)^{n-1}$ compared to the drop in elasticity of $(1-D)$. The result is a decrease in the Maxwell time of the margins, meaning that the viscous response would be relatively more important. However, if *En* is assumed to be constant between the viscous and elastic enhancement, then the Maxwell time is unaffected in the marginal ice, suggesting that viscoelastic deformation is no more important in the margins than in the central ice. Finally, if the presence of crevassing has a larger effect on the elasticity relative to the viscosity, then the Maxwell time of the margins would be increased relative to the undamaged ice, suggesting that viscoelastic deformation would be most important in the undamaged portions of the ice stream. A more complete understanding of the role of damage in influencing the viscoelastic deformation of ice is necessary to have a physically based model for viscoelastic damage in the shear margins. While it is possible to approach the problem of viscoelastic damage in the same manner as we did for elastic damage, the increased computational time of the nonlinear viscoelastic models puts such an effort well beyond the scope of this chapter.

3.3.2 Homogeneous Viscoelastic Modeling Results

We describe results from three viscoelastic models using homogeneous viscosity (assuming 0 °C ice) and tidal frequencies corresponding to the semidiurnal, diurnal, and fortnightly ocean tides. Recall that for each model, two versions are run: one with only

the background gravitational body force ("background model") and a second with both the background force and the axial tidal load ("tidal model"). Figure 3.12 shows a sample stress field for the basal profile of the semidiurnal tidal model at the peak tidal amplitude with the background model subtracted. Qualitatively, the stress distribution for the viscoelasticity model is similar to that of the elastic model (figure 2.6), though there are clearly some differences in the shear margins of the ice stream. The value of L_{tr} can be seen in multiple stress components and does not vary substantially between the different stress components. As with the elastic model, tidal stress decays exponentially with distance inland, and while the peak normal stress occurs in the center of the ice stream, the decay length-scale L_{tr} is roughly constant across the ice stream's profile.

Figures 3.13 to 3.15 show the value of L_{tr} as a function of depth at the centerline of the ice stream for the models forced at the three tidal frequencies. As seen in panels A, the stress-transmission length-scale does not vary greatly with depth for any of the models. However, the value of L_{tr} varies with the period of the forcing frequency. For the semidiurnal, diurnal, and fortnightly tides, the length-scales are 15.6 kilometers, 15.0 kilometers, and 40.9 kilometers, respectively. L_{tr} for the corresponding elastic model is 12.2 km, meaning such viscoelastic values of L_{tr} correspond to 123%, 118%, and 335% of the elastic value. Thus, using viscoelasticity does increase the extent of tidal stress-transmission relative to the elastic model.

Another major change in the move from elasticity to viscoelasticity is that we must consider the time-history of the stress solution, not just the stress state at a single moment. As a demonstration, figure 3.15 compares the value of σ_{yy} at the base of the center of the model ice stream forced with the semidiurnal tide as a function of time at

several locations inland of the grounding line. In addition to the decay of the stress amplitude with distance inland of the grounding line, there is a phase delay in the ice stream's stress response to the tidal load that also varies with distance inland of the grounding line. In order to find the correct amplitude and phase, we fit stress profiles along the modeled ice stream's length with:

$$\sigma_{yy} = A\sin(\omega t + \varphi) \tag{3.15}$$

where A is the stress amplitude, ω is the tidal frequency of the applied tide, and φ is the phase delay. Panels B and C of figure 3.12 to 3.14 show the fitted amplitudes and phase delays for the centerline profiles over of the ice stream model over the first 100 kilometers of the ice stream. The dashed lines correspond to the 95% confidence intervals of the fits. The slopes of the amplitude and phase are the values of the length-scale for the decay of the tidal stress, L_{tr}, and the phase velocity, c, respectively. Table 6.3 summarizes the values of L_{tr} and c for the homogeneous models.

The ice stream's response to all three forcing frequencies displays a phase delay that increases with distance away from the grounding line, as seen in panel C. However, the phase does not seem to correlate with L_{tr} in these models. The phase velocities of the three tides are, in order of increasing tidal period, 4.6 m/s, 11.1 m/s, and 0.60 m/s. The phase velocities are not monotonically increasing with tidal period as the fortnightly tide has a significantly longer tidal period than the shorter period tides, but not a significantly increased phase delay.

3.3.3 Temperature-Dependent Viscosity Results

For our temperature-dependent viscosity models, we present results for the isolated semidiurnal, diurnal, and fortnightly tidal components, as well as a single model that

forces the models with a combined tidal forcing function based on the amplitudes of the Weddel Sea's tides (see Table 3.2). Figures 3.17 to 3.20 show the values of L_{tr}, stress, and phase delay for the semidiurnal, diurnal, fortnightly, and combined tidal signal.

As with the homogeneous viscosity model, all three viscoelastic models have larger values of L_{tr} than the homogeneous elastic model. The fortnightly tide has a longer L_{tr} than the other two tides while the diurnal tide in turn has a larger value of L_{tr} than the semidiurnal tide. Additionally, the absolute amplitude of the change is less pronounced than in the homogeneous case, with the semidiurnal L_{tr} being 101% of the elastic case, the diurnal tide's L_{tr} being about 102%, and the fortnightly tide's L_{tr} being 145%.

In all three cases, the phase delay at the grounding line is zero degrees, suggesting a purely elastic response. The phase delay increases with inland distance, with the maximum phase delay reaching about 15 degrees for the semidiurnal tide, 90 degrees for the diurnal tide, and 270 degrees for the fortnightly tide. Unlike the homogeneous model, the increase in the phase delay correlates with an increase in L_{tr}. Such is a result is due to the increased average viscosity, and thus the value of T_{max}, of the temperature-dependent ice stream relative to the homogeneous ice stream. We discuss the phase response to the ocean tides further in chapter 4. Finally, the phase velocities of the three tides are 1.8 m/s, 1.7 m/s, and 0.94 m/s for the semidiurnal, diurnal, and fortnightly tides, respectively.

3.3.4 Viscoelasticity Discussion

Our primary interest in modeling viscoelasticity was to determine if stress-dependence of viscosity would result in a substantial decoupling of the ice stream from its lateral margins due to the higher stress concentration along the lateral margins. Recalling our earlier comparisons to the estimated tidal stress decay over Bindschadler and Rutford Ice

Streams (figure 2.11), viscoelasticity would need to increase the value of L_{tr} by between a factor of two to five to match the field observations of Anandakrishanan et al. (2003) and Gudmundsson (2007; 2008; 2011). While models with a homogeneous viscosity at long tidal periods have values of L_{tr} that fall into the range necessary to fit the Antarctic observations, incorporating a temperature-dependency to the viscosity severely diminishes the increase in L_{tr} relative to the elastic model. For these temperature-dependent models, the increase in L_{tr} is less than 50%—insufficient to match the observations.

The lack of a substantial increase in L_{tr} due to the ice viscosity calls into question our assumption that incorporating nonlinear viscoelasticity will substantially reduce the viscosity in the shear margins. However, as figure 3.20 shows, the shear margins have a substantially reduced viscosity when compared to the central ice. This viscosity contrast is found to be essentially independent of the tidal forcing, suggesting that the background flow, even for very low driving stresses, is large enough that the tidal forcing does not strongly perturb the effective ice viscosity. As such, response of an ice stream to a tidal load can be approximated as a linear viscoelastic as long as the ice stream is modeled with a spatially variable effective linear viscosity. Such a simplification allows the use of the principle of linear superposition and thus decouples the effects of the tides from any background stresses. Clearly linear models are also less computationally expensive, allowing us to explore a wider range of model parameters.

However, the large drop in viscosity in the shear margins fails to cause a substantial increase in L_{tr}. The simplest explanation is that while the ice is less viscous in the shear margins, the overall value of the viscosity is too still large to promote

substantial viscous deformation. When compared with approximations of linear ice viscosities, the smallest viscosities in our models are about two orders of magnitude larger than those found for the solid response of laboratory ice (e.g., *1e12 Pa·s*, from Jellinek and Brill, 1956). As the smallest Maxwell time for our modeled ice stream is about 10^4 seconds (~ 3 hours), the model ice stream responds primarily as an elastic material. Only when the model is forced with long period oscillations (e.g., the fortnightly tide, with a period of ~ 10^6 seconds) does the viscoelasticity of the ice stream substantial influence the stress-transmission length-scale. Such an explanation matches the modeling result that a temperature-dependent viscosity has a smaller impact on the transmission length-scale than the equivalent homogeneous model. As our homogeneous model is calibrated to match ice at the melting point, the homogeneous model has an average effective viscosity that is about 30 times smaller than the average effective viscosity in the temperature-dependent model. For the temperature-dependent models, the larger viscosity in the body causes the ice response to be more elastic in nature, explaining the diminished change in L_{tr} from the viscoelastic model.

Our results demonstrate that a viscoelastic ice stream will have a phase delay in the ice's response to a tidal loading that is distance dependent, whereas a linear elastic ice stream will never have an induced tidal phase delay. While our results are too limited to draw any sweeping conclusions about the interplay between the phase delay, tidal forcing frequency, and the effective viscosity of the ice, the results do suggest that a measureable phase delay in the tidal response can provide information about the viscoelastic behavior of the ice. We explore this idea further in the next chapter.

3.4 Summary and Conclusions

We explored changes in the overall state of stress in an ice stream due to two different rheological modifications to a homogeneous linear elastic rheology. The goal was to determine if either an increased elastic compliance in the shear margins or nonlinear viscoelastic effects would decouple the ice stream from its lateral margins to such an extent as to explain the discrepancy between the short stress-transmission length-scales of our models with the large spatial extent of tidally perturbed surface displacement observations from some Antarctic ice streams. We find that neither of these two rheological effects have sufficient input on estimates of L_{tr} to explain differences between our models and observations.

The first portion of this chapter considered models using a linear continuum damage mechanics formulation of crevassing in the highly-deformed shear margins of ice streams to reduce the margins' effective elasticity. Our models demonstrated that the resulting inhomogeneity in ice elasticity causes a net increase in L_{tr} for a tidal load if the marginal ice is more compliant than the central ice. While a perfect constraint on the damage in the ice stream margins is not well established, we assume that the upper bound on damage for ice calving is an approximate bound on the marginal damage. Using this constraint, the magnitude of the damage necessary to rectify the observations and our model results must be unrealistically large.

The second rheological consideration is the impact of incorporating a nonlinear viscoelastic constitutive law for ice instead of the linear elastic law used in chapter 2. The hypothesis was that the stress-dependent viscous component of the viscoelastic rheology would decouple the ice stream from surrounding ice by reducing the viscosity

of the shear margins due to the large shear stresses in these margins. Our viscoelastic models demonstrated that generally, viscoelasticity increases L_{tr} and that the viscous response is stronger for longer period tidal forcings. However, for a model incorporating the temperature dependence of the viscosity coefficient of the ice stream approximating the temperature profile of Antarctic ice streams, viscosity remains too large to increase the stress-transmission length-scale of tidal load by more than about 50% compared to the elastic model. Ultimately, due to the low driving stresses that control the magnitude of the effective viscosity within the model ice stream, for the Antarctic ice streams of interest, viscoelasticity cannot increase L_{tr} enough to rectify the observations and the model results.

Figure 3.21, an updated version of figure 2.11, demonstrates graphically that the decay of displacements is still too severe to match the maximum observed displacement if the influence of physically reasonable damage or viscoelasticity is added to our models. Recall that for linear elasticity, an exponential decay of stress corresponds to an exponential decay of displacement with the same decay length-scale. Thus, using a value of L_{tr} calculated from the tidal stress-transmission can be used to represent the decay of tidally induced displacements with distance inland of the grounding line. For nonlinear viscoelastic models, as the total stress state is dominated by the elastically supported stresses it is still reasonable to approximate the displacement decay using the stress-transmission length-scale. The estimated L_{tr} for elastic model geometries approximating Bindschadler and Rutford Ice Streams are approximately 70 and 40 kilometers, respectively (GPS data reported in Anandakrishnan and others, 2003; Gudmundsson, 2007 and was provided by S. Anandakrishnan and H. Gudmundsson). The increase in

the stress-transmission length-scale is 60% for the maximum reasonable damage model. In our viscoelastic models, the increase in L_{tr} for the semidiurnal tidal forcing is about 1% while for the fortnightly forcing the increase in L_{tr} is about 45%. Such values are insufficient to match the observed stress-transmission length-scales of 265 and 110 kilometers, respectively for Bindschadler and Rutford Ice Streams.

The models presented here draw into question the hypothesis that the observed influence of ocean tides on ice stream motion occurs as elastic transmission through the bulk of the ice stream itself. This result implies one of two possible conclusions: one, that there is a mechanism not explored here that almost completely decouples the ice stream from its shear margins, essentially reducing the lateral support of the ice stream to zero; or two, that a mechanism external to the ice stream bulk is necessary to explain the tidal component of ice stream motion. The uniform flow-line models, which are the current state-of-the-art, implicitly assume the first, though we have demonstrated here that the ice streams considered here are not wide "enough" to neglect the resistance of the lateral margins. Furthermore, even the very name of the shear margins implies that there must be an amount of lateral support sufficient to induce shear in the ice stream's margins, making large-scale decoupling very unlikely.

Thus, we conclude that a process external to the ice stream is the most likely mechanism for allowing the impact of ocean tidal loads to extend far inland of the grounding line. While not explored in detail here, our preferred hypothesis is that the ocean tides perturb the nature of streaming through the subglacial hydrologic network. As the basal traction beneath these fast-moving ice streams must be small as to encourage sliding and as these Antarctic ice streams are underlain by water-logged tills (e.g., Alley

et al, 1986; Smith, 1997; Engelhardt and Kamb, 1998; Tulaczyk et al., 2000a; Adalgeirsdottir et al., 2008; Raymond Pralong and Gudmundsson, 2011), the fluid pressure within the subglacial till is likely sufficient to cause the till to deform plastically. Our hypothesis is that the change in ocean tidal height can move the onset of streaming, the transition from slow- to fast-moving ice at the upstream edge of the ice stream, inland and seaward over the course of a tidal cycle. As demonstrated by figure 3.22, when the onset of streaming is pushed inland, the ice stream at a given point should increase velocity as a longer portion of the glacier is streaming. The opposite is true when the onset of streaming moves towards the ocean. Furthermore, as the magnitude of the fluid pressure perturbation due to the ocean tide should decay with distance inland of the grounding line, the effect is expect to be most pronounced near the grounding line. Perhaps this distance dependence on the subglacial tidal pressure could explain the phase delay between ocean amplitude and the ice stream's response to changes in ocean tide.

The distance the tidal pressure change travels could easily be farther inland than the 5 kilometers zone through which the grounding line moves due to the ocean tides (e.g., Stephenson, 1984; Rignot, 1998; Heinert and Riedel, 2007; Brunt et al., 2010). As the water pressure within the basal till is not constrained by the ice stream's width (the ice stream dimensions controlling L_{tr}) but rather by the hydraulic properties of the subglacial drainage network, such a pressure modulation could potentially reach farther inland than a tidal load acting through the bulk of the ice stream does. However, any further discussion of such a process relies on quantifying the spatial extent that ocean tides are 'felt' through the subglacial hydrologic network, which is beyond the scope of this chapter.

	Variable Names	Units
A	Viscosity coefficient	$Pa^{-n}\ s^{-1}$
a	Accumulation rate	kg/yr
C	Phase velocity	m/s
D	Damage parameter	--
D_C	Critical damage parameter	--
D_1	Viscous damage parameter	--
D_2	Elastic damage parameter	--
De	Deborah number	--
E	Young's modulus	Pa
E_{eff}	Effective Young's modulus	Pa
E_H	Higher Young's modulus	Pa
E_L	Lower Young's modulus	Pa
En	Enhancement factor	==
g	Gravitational acceleration	$m\ s^{-2}$
g_{horiz}	Horizontal component of gravitation acceleration	$m\ s^{-2}$
H	Ice stream thickness	m
H_I	Cliff height	m
L_{tr}	Stress-transmission length-scale	km
l	Diffusion length-scale	km
N	Stress exponent	--
q_b	Basal temperature gradient	°C/m
T	Temperature	°C
T_{max}	Maxwell relaxation time	s
T	Time	s
t_f	Forcing timescale	s
u	Ice stream velocity	m/s
x	Ice stream transverse coordinate	km
y	Dimensionless depth	--
Z	Depth	m
α	Surface slope	°
ε	Strain	--
η	Viscosity	Pa s
κ	Thermal diffusivity	$m^2\ s$
λ	Temperature gradient in air	°C/m
ν	Poisson's ratio	--
ρ	Ice density	$kg\ m^{-3}$
σ	Stress	Pa
σ_{ij}	Stress component	Pa
σ_{trans}	Transitional stress	Pa
τ_b	Basal stress	Pa
φ	Phase delay	°
ω	Forcing frequency	s^{-1}
"$\bar{}$"	Normalized quantity	
"$\hat{}$"	Non-dimensionalized quantity	

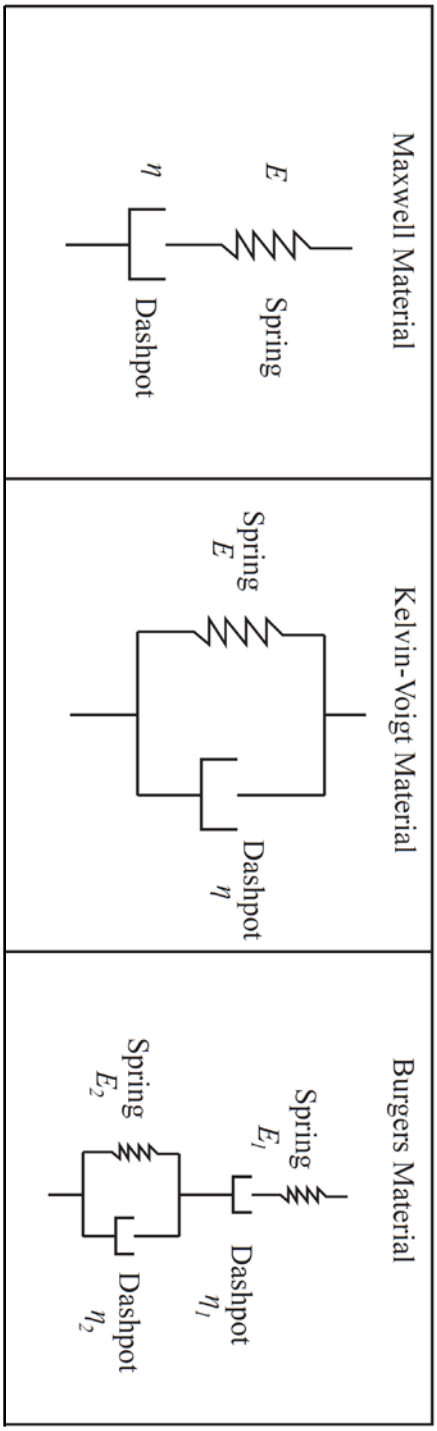

Figure 3.1: Schematic views of the one-dimensional Maxwell, Kelvin-Voigt, and Burgers viscoelastic models. The models are made up of spring and dashpot elements, with the associated moduli shown next to each element.

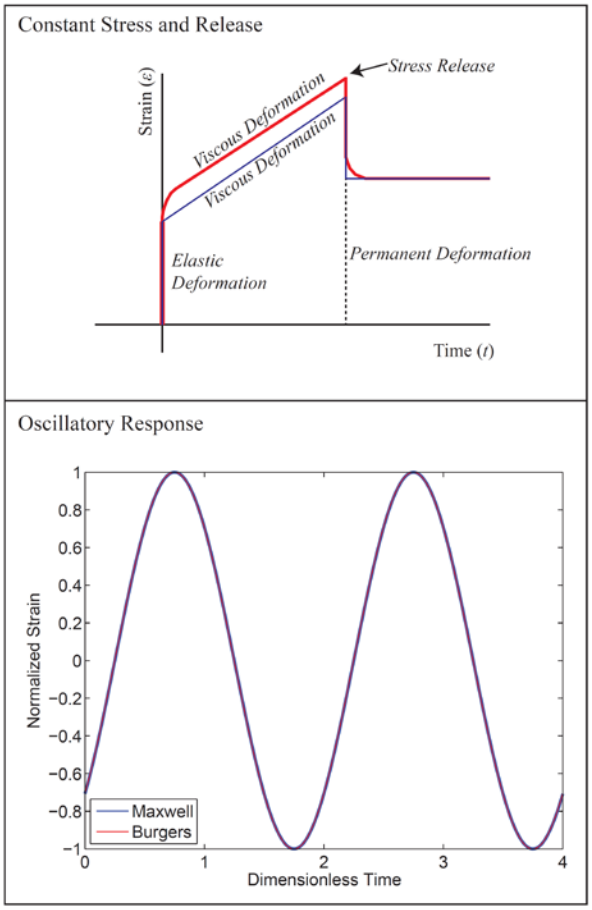

Figure 3.2: Comparison of the response of a one-dimensional Maxwell (blue) and Burgers model (red). In the upper panel, a constant stress is applied to the two materials, and the released at an arbitrary time. The Burgers model has a tapered response due to the solid element, but converges on the Maxwell model's response. In the lower panel, the oscillatory response of a Maxwell material and the response of a Burgers material are plotted as a function of dimensionless time. The Burgers model has a Kelvin-Voigt element that has a retardation time that is 100 times smaller than the relaxation time of the Maxwell material. Such a model is a approximately what is expected for ice (e.g., Jellinek and Brill, 1956). The oscillatory responses of the two rheologies are negligibly different.

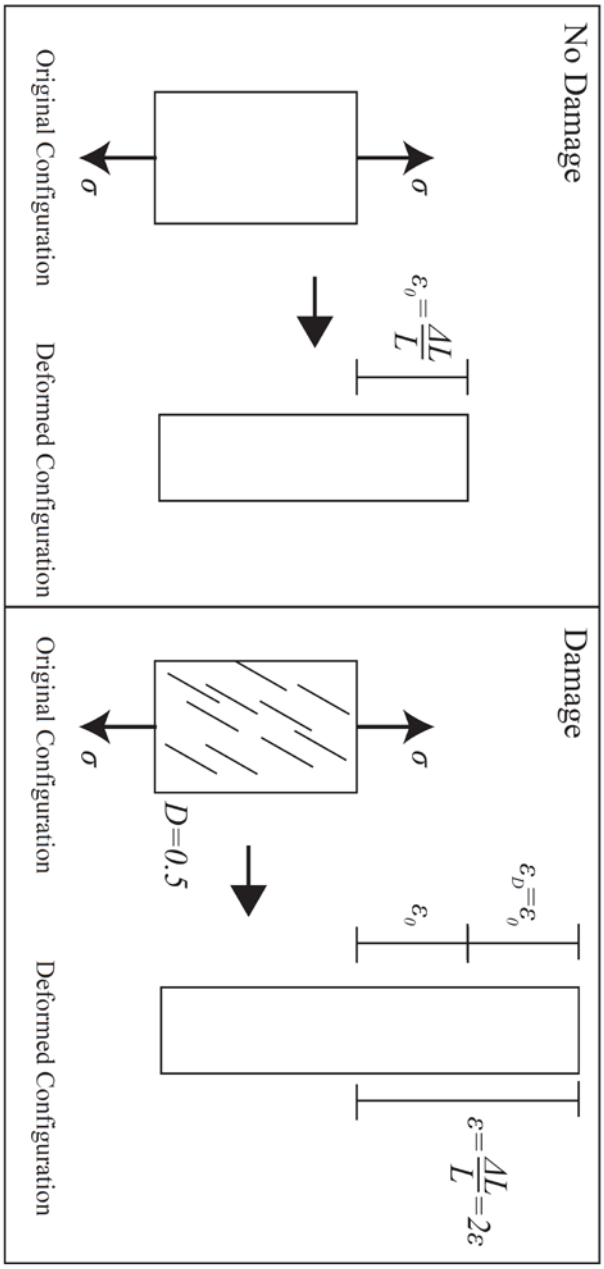

Figure 3.3: Schematic of the continuum damage mechanics formulation. The left panel shows the undamaged uniaxial strain of an elastic material. The right panel shows the strain of a damaged version of the same uniaxial strain. As the damage parameter in this example is chosen to be *D=0.5*, the total strain is twice the undamaged version, as the effective Young's modulus of the damaged material is $E_{eff} = (1 - D)E = 0.5E$.

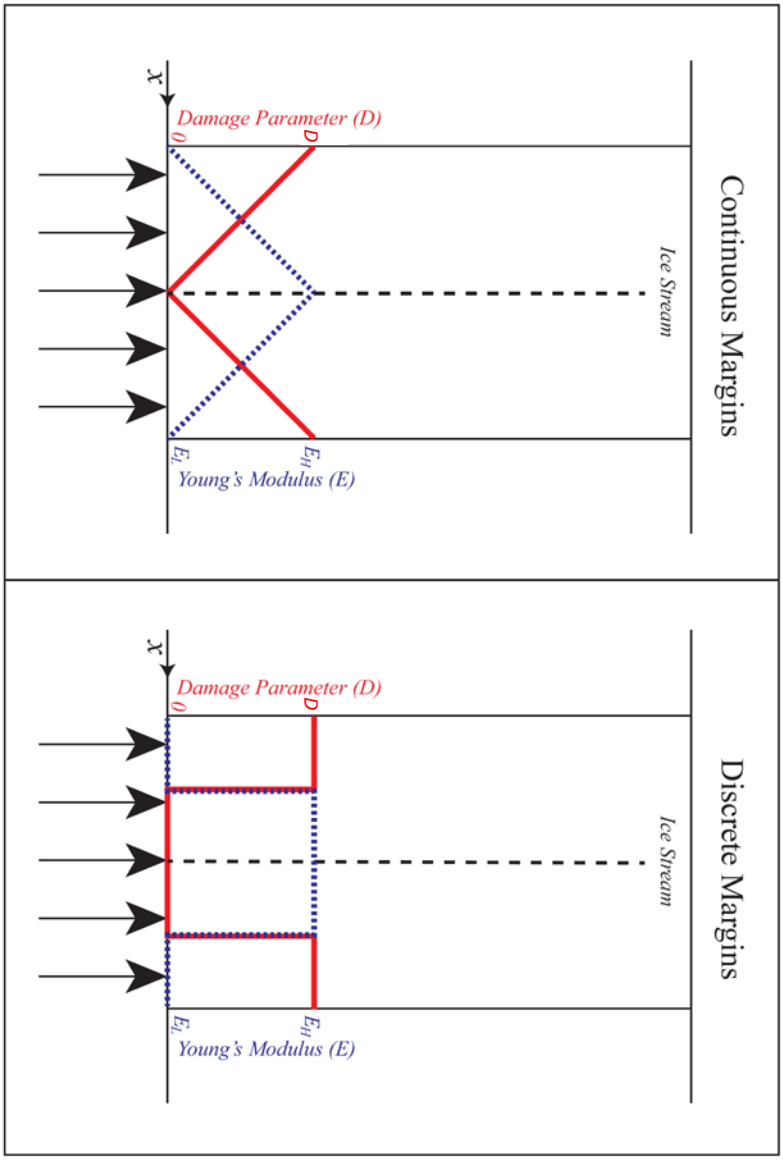

Figure 3.4: Diagram of the elasticity and damage profiles used in our marginal analysis models. The panel on the left shows the continuous margin model, while the right panel shows the discrete margin model. In each panel, the damage parameter D is plotted in red while the effective Young's modulus E is plotted in blue. The profiles are constant with inland distance of the grounding line. The grounding line is marked with arrows, as the grounding line is the location of the applied tidal forcing.

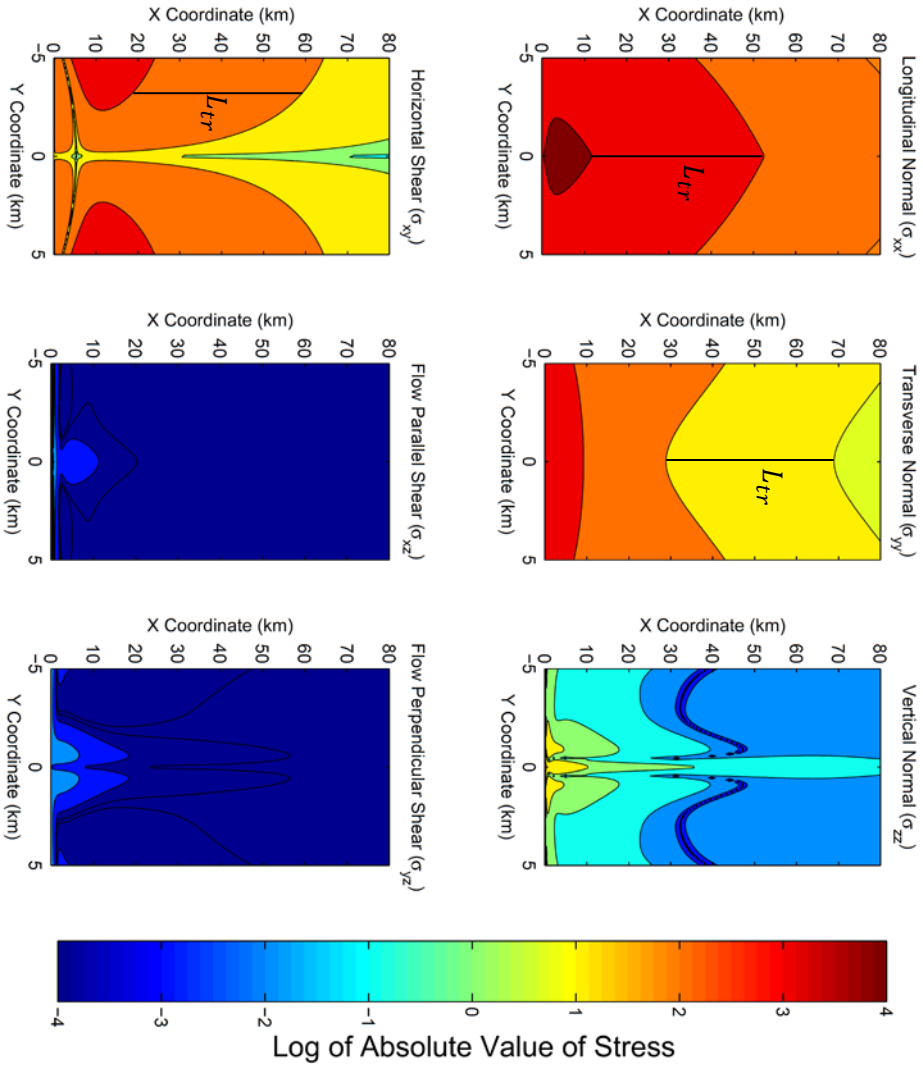

Figure 3.5: Representative stress state for a continuous margin model that has a one order of magnitude variation in Young's modulus between the central (strong) ice and the marginal (weak) ice. The transmission length-scale L_{tr} is shown on some of the stress components. Note that near the grounding line, the stress is elevated, but that away from the grounding line, the value of L_{tr} is constant along the transverse profile of the ice stream.

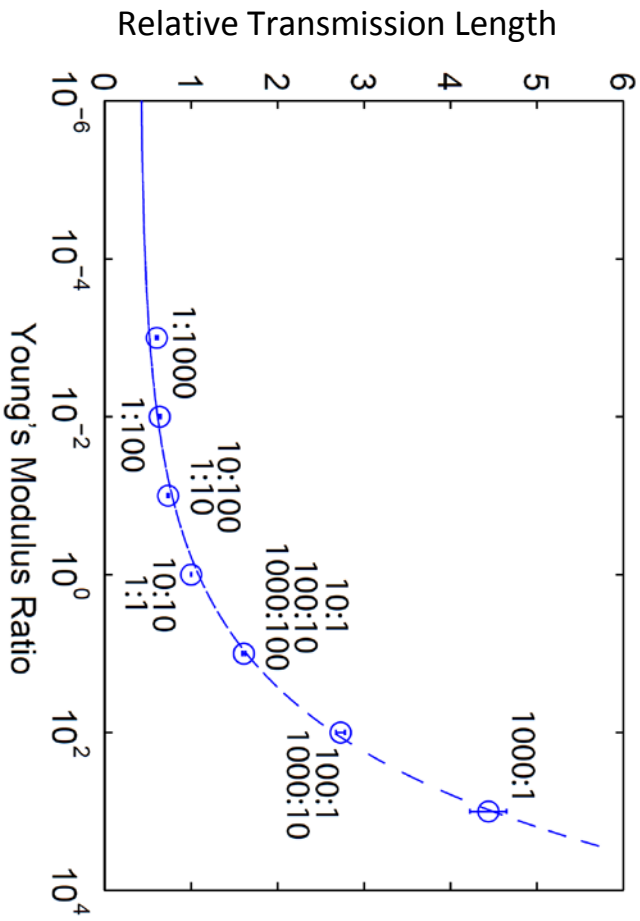

Figure 3.6: Change in average L_{tr} increase for models with continuous margins as a function of relative Young's moduli between the margins and central ice. The relati values of central Young's modulus, E_H, and marginal Young's modulus, E_L, listed n the corresponding data point. Error bars represent one standard error of the mean. T dashed line is a best-fit power law function. The equation for the fit is: $\hat{L}_{tr} = 0.699 * 1.790^{\log(\hat{E})} + 0.392$, where $\hat{E}$ is the ratio of the Young's modulus in the central ice divided by the Young's modulus of the lateral margins.

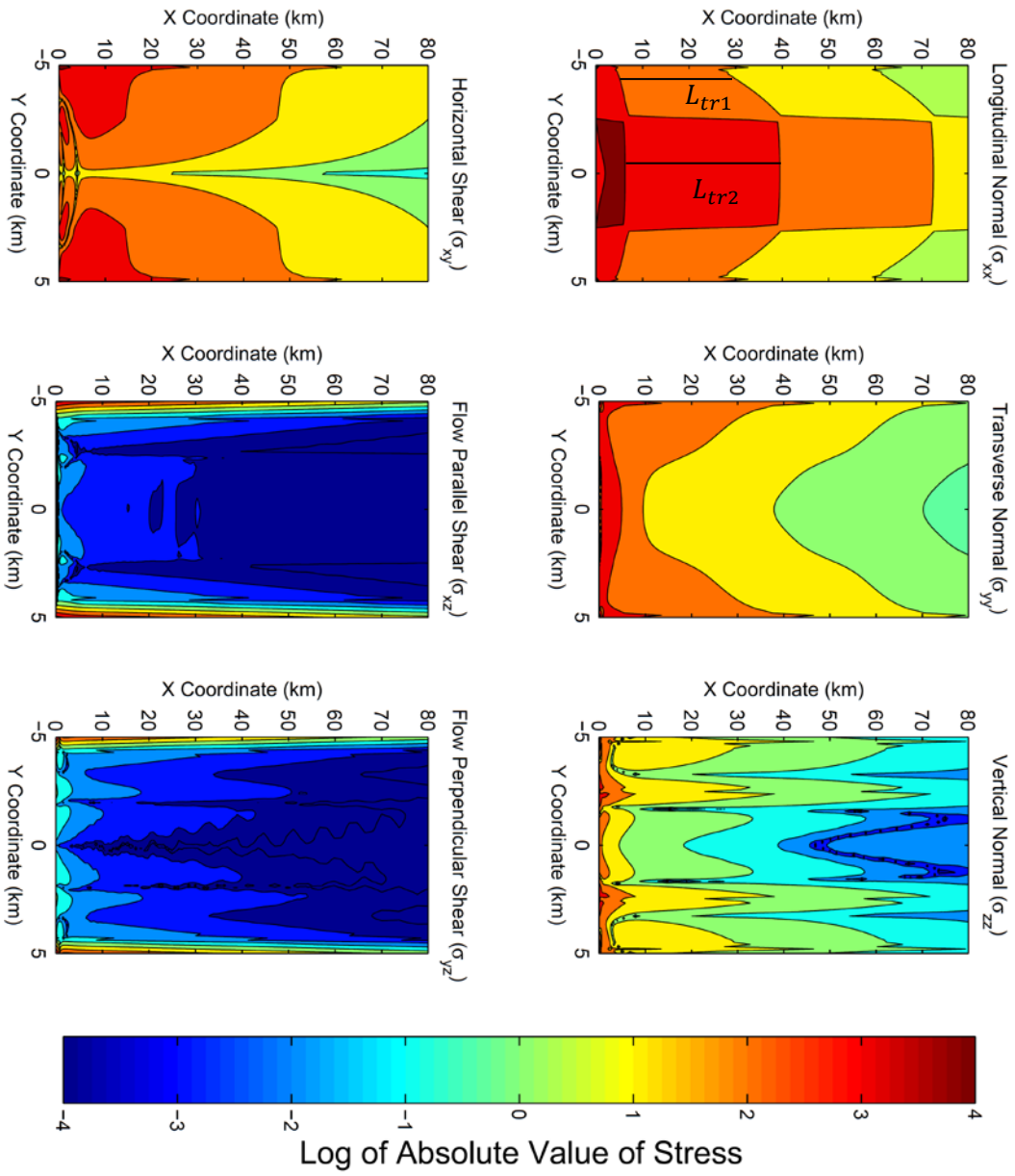

Figure 3.7: Representative stress distribution for a model with the same geometry as figures 2.6 and 3.5, but with ice margins that are one quarter of the ice stream's total width. These margins are a factor of 10 more compliant than the central ice. A variable L_{tr} as a function of transverse location is highlighted in the σ_{xx} component of stress.

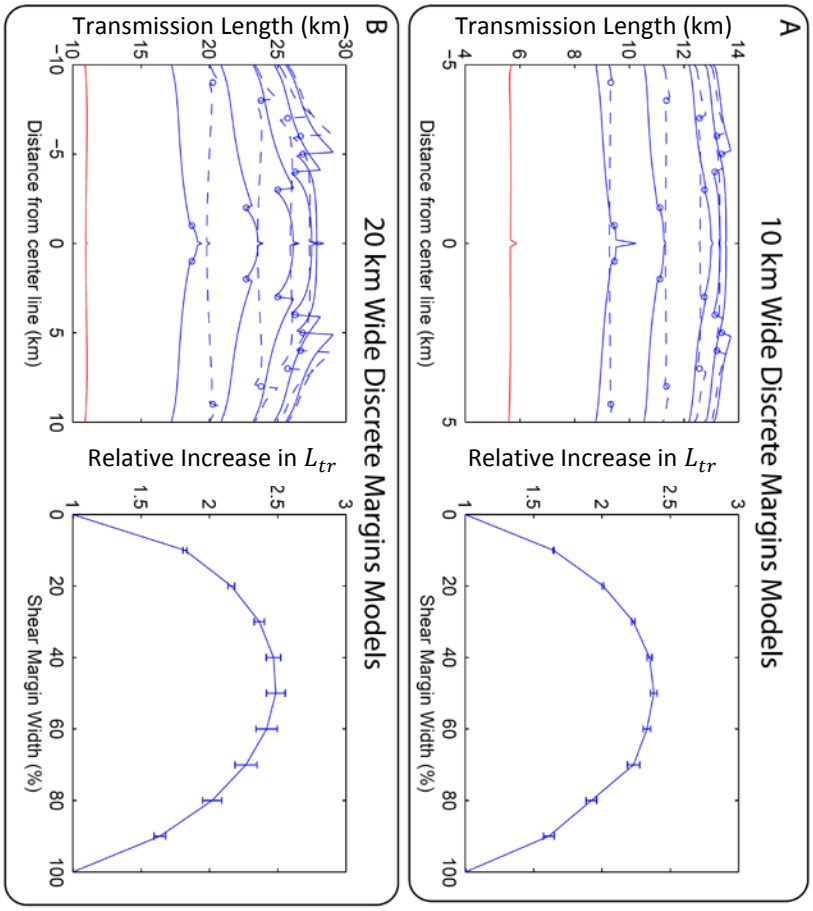

Figure 3.8: The relationship between the marginal width and L_{tr} compared to a uniform model for discrete margins. Top figures are for a model 10 kilometers wide, while bottom figures are for a model 20 kilometers wide. Figures on the left show the transverse profile of $L_{tr,}$ with select profiles dashed to aid with visibility. Circles represent the location of the edge of the ice margins. The models that have homogeneous elasticity (0% and 100% width shear margins) are plotted in red. Figures on the right show the increase of the relative values of L_{tr} as a function of shear margin width. The error bars indicate one standard error of the mean. The fit for figure 3.8B, as described in the main test, is: $\hat{L}_{tr} = \frac{L_{tr}}{L_{tr,homog}} = -11.94\hat{x}^4 + 25.45\hat{x}^3 - 23.14\hat{x}^2 + 9.64\hat{x} + 1$, where $\hat{x}$ is the non-dimensional width of the marginal shear zone, ranging from 0 to 1.

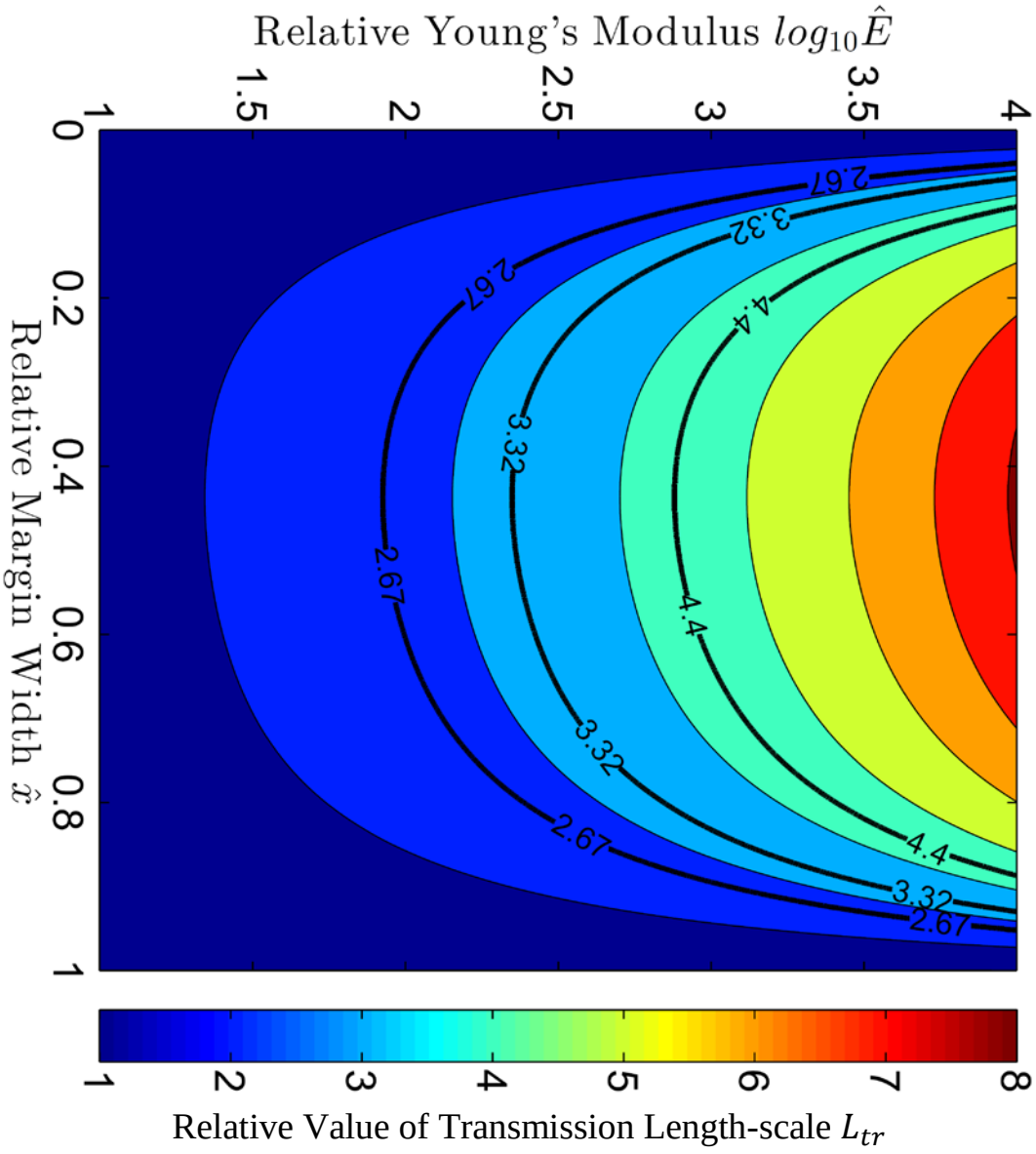

Figure 3.9: Young's modulus and margin width space for the increase in L_{tr} for a discrete margin model relative to the homogeneous elastic model described in chapter 2. The three bolded contours correspond to the conditions necessary to single-handedly explain the observations of the Rutford fortnightly tidal signal 4(2.67), the Rutford semidiurnal tidal signal (3.32), and the Bindschadler semidiurnal tide (4.40).

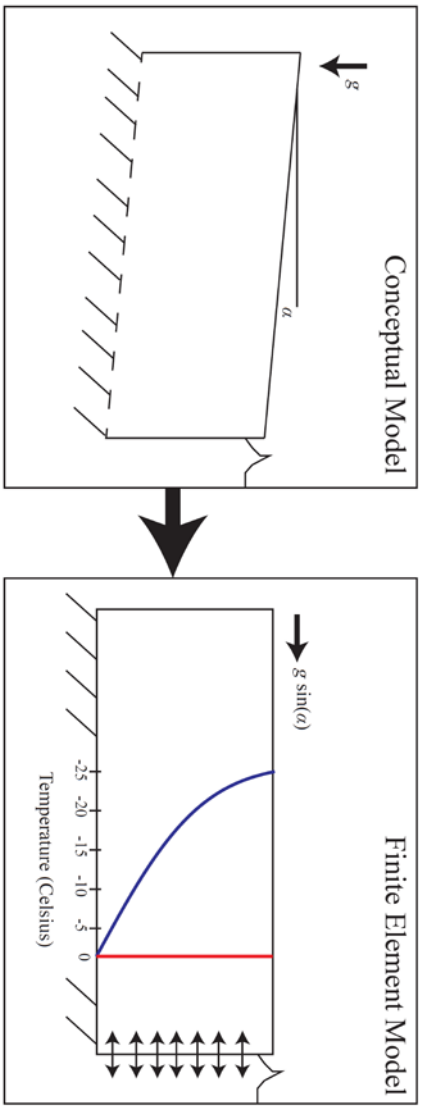

Figure 3.10: Conceptual and finite element model implementation of the gravitational driving stress. While in the conceptual model, there is a surface slope α, this is approximated by applying the deviatoric (horizontal) component of the gravitational acceleration, with a magnitude of $g \sin \alpha$. The finite element model also shows the two temperature profiles used in our viscoelastic models. The red line is the homogeneous temperature profile at $0\ ^{\circ}C$, while the blue curve is the temperature profile defined in equation 3.14.

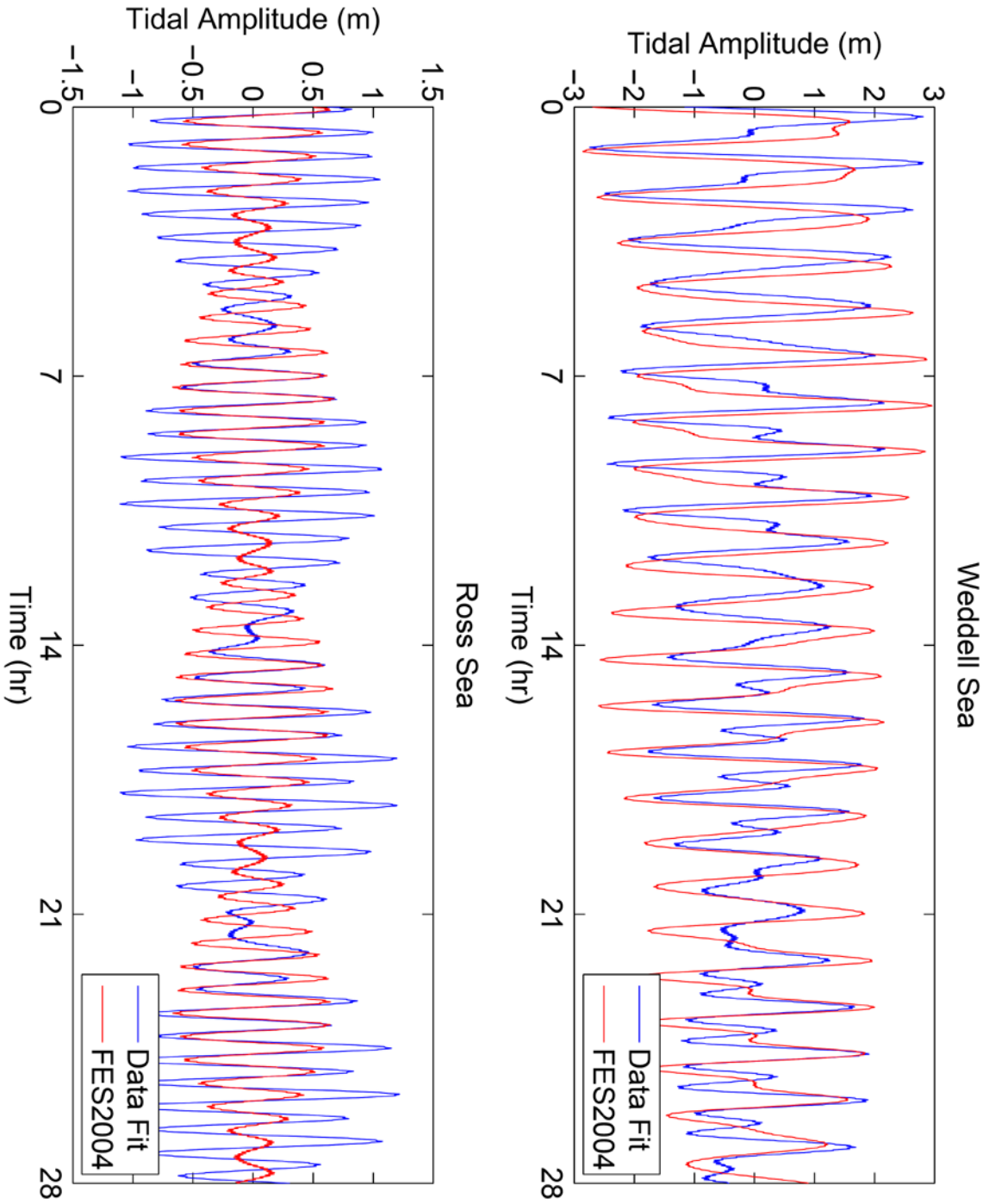

Figure 3.11: Comparison of the global tidal model FES2004 (red) to a five-component fit of tide-height data (blue) from the Weddell and Ross Seas. Tidal amplitudes and phases are listed in table 3.2.

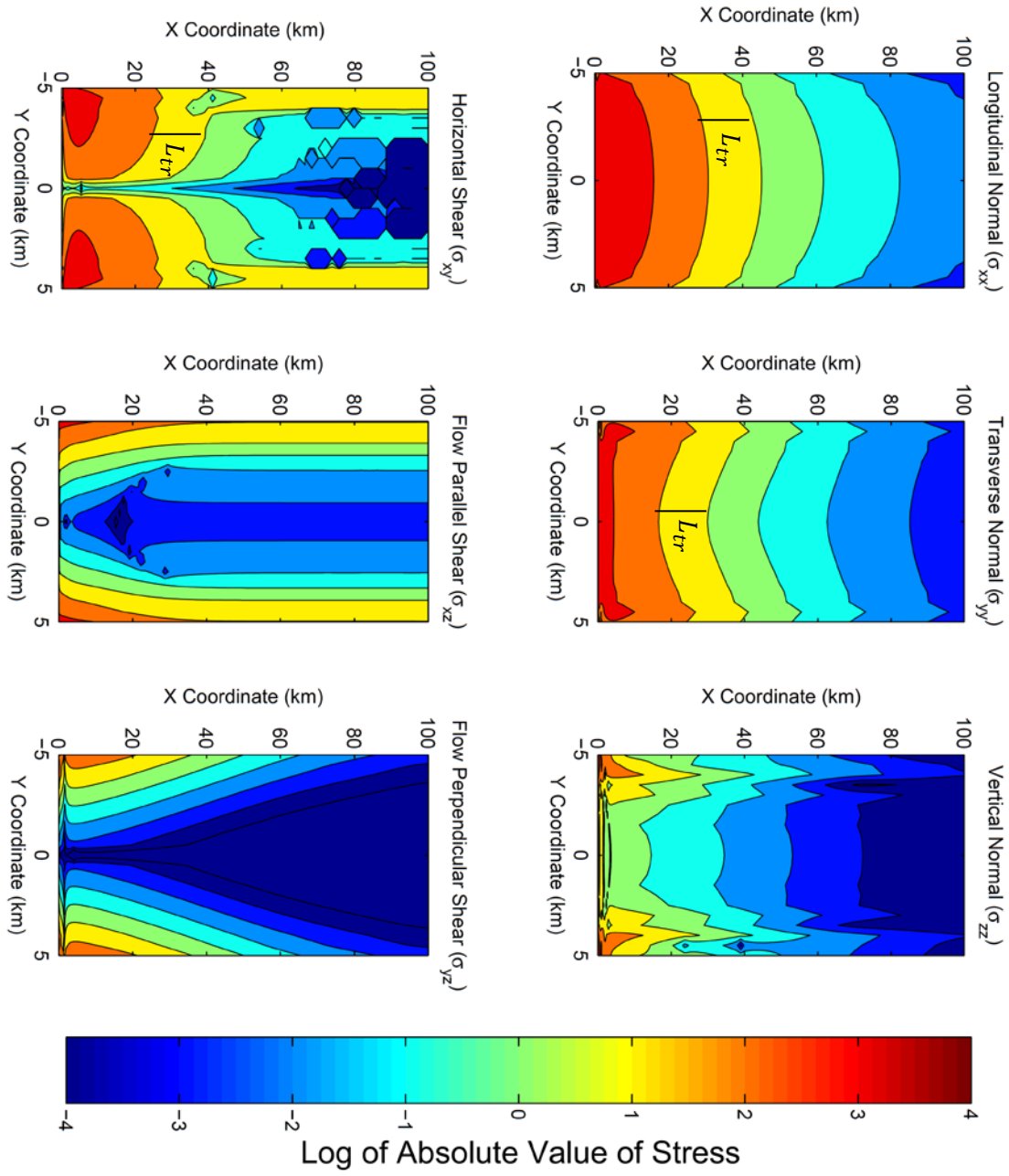

Figure 3.12: Stress state at the base of a modeled ice stream ten kilometers wide, one kilometer thick, and forced by a semidiurnal one meter tide. The stress values plotted are the "tidal" model with a "background" model subtracted, as discussed in section 3.3.4. The physical length of L_{tr} is drawn on the stress components where such a distance is easily seen.

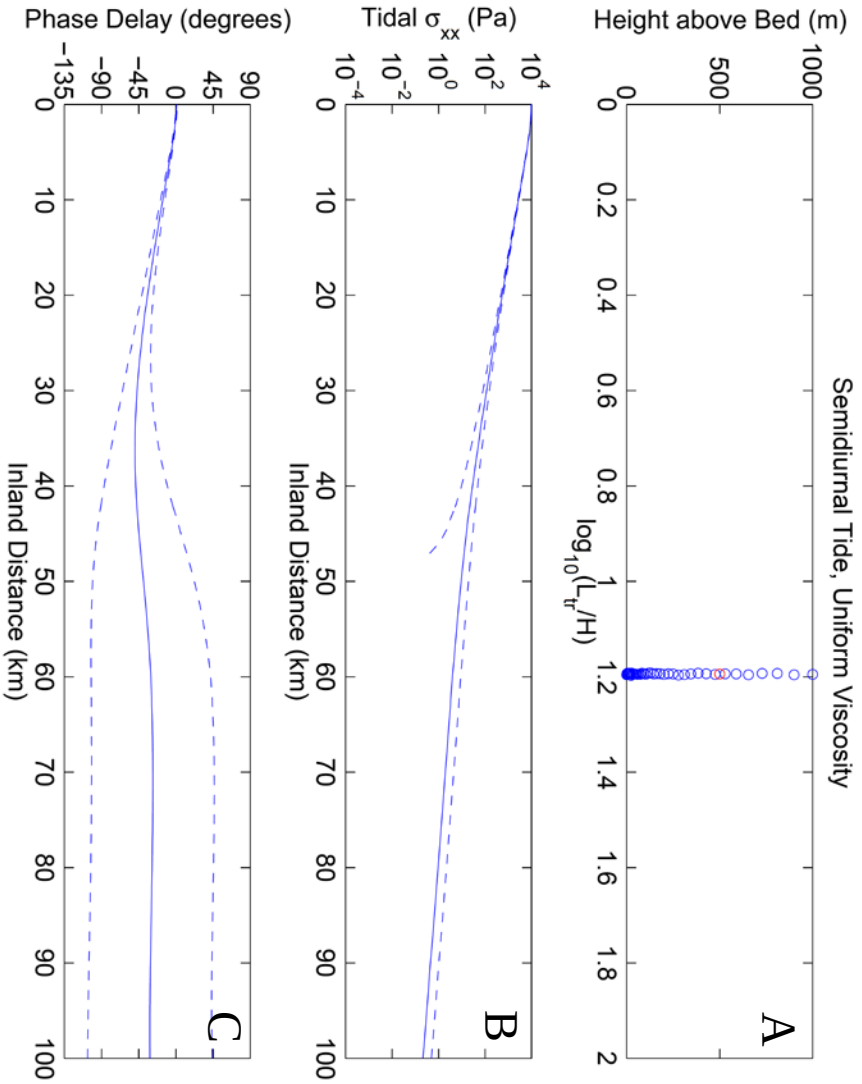

Figure 3.13: Model results for a viscoelastic model with a uniform temperature profile that is forced by a semidiurnal tide. Panel A shows the calculated values of L_{tr} for depth profiles of the stress. The average value of L_{tr} is 15.63±0.04 km. Panel B shows the value of the longitudinal normal stress (σ_{yy}) as a function of horizontal coordinate. Panel C shows the fitted phase shift φ as a function of horizontal coordinate. In panels B and C, the dashed lines correspond to the 95% confidence interval values of the fit described in equation 3.15.

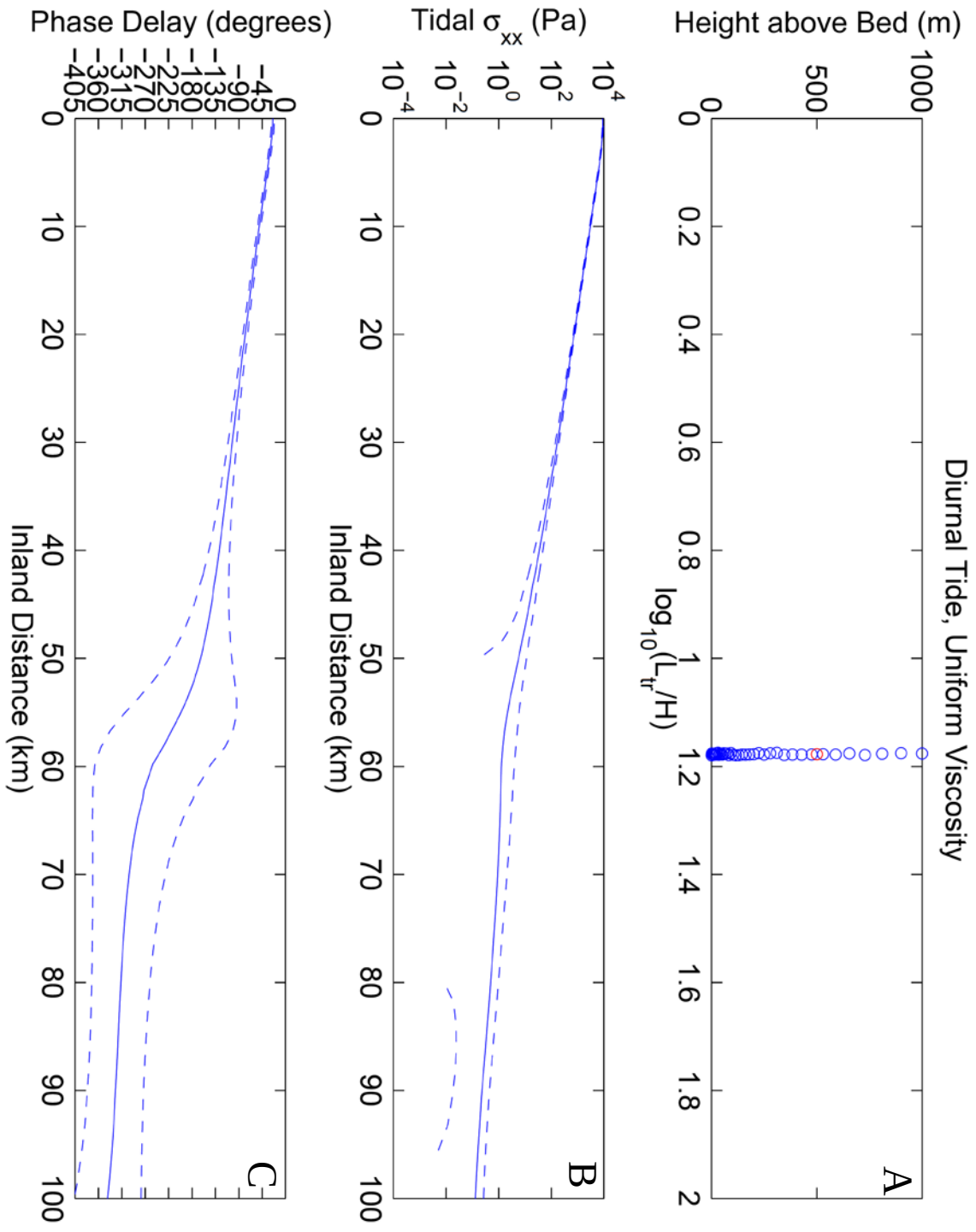

Figure 3.14: Model results for a homogeneous viscoelastic model forced by a diurnal tide. The values in the three panels match the description in figure 3.13. The average value of L_{tr} is 15.04±0.04 km.

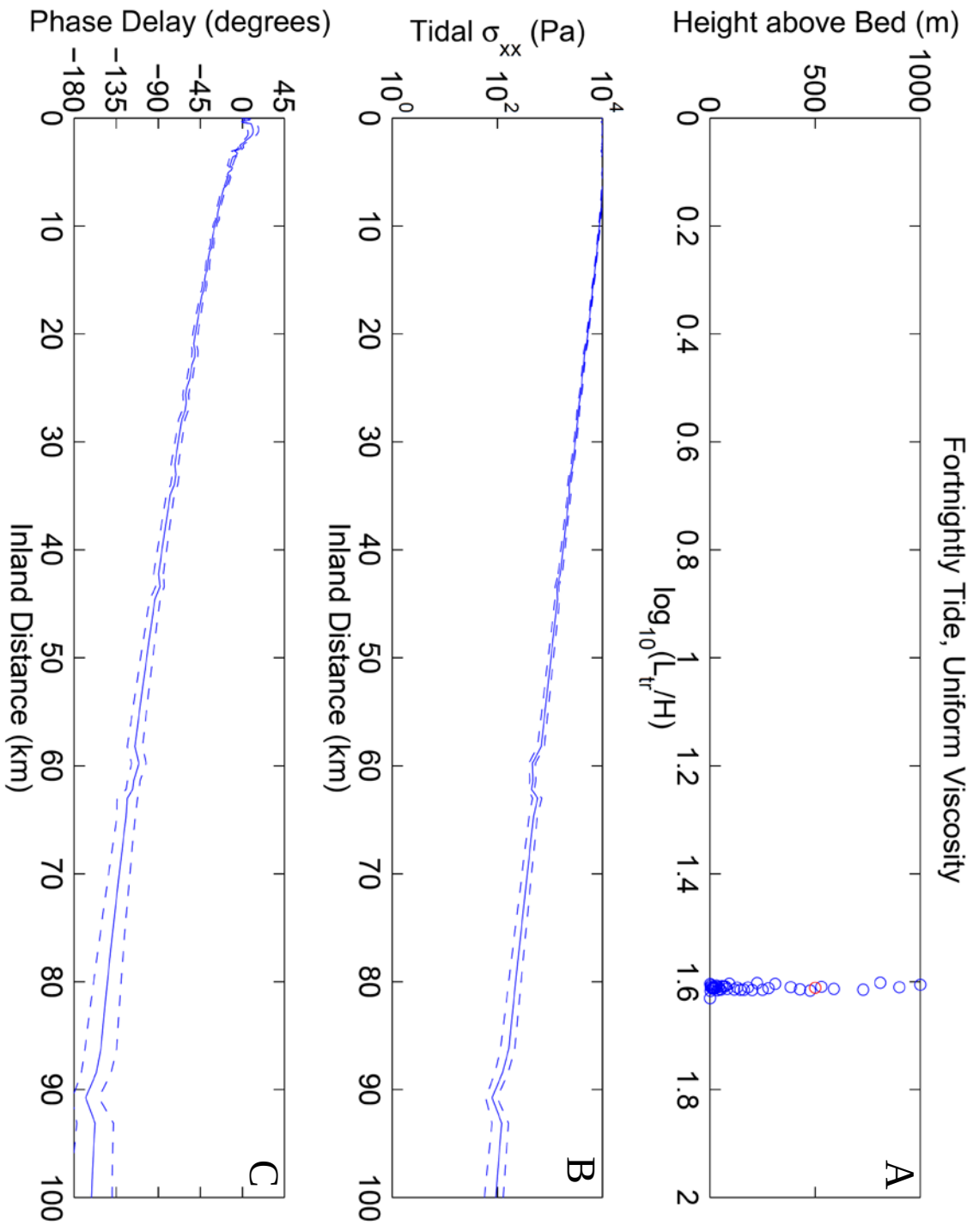

Figure 3.15: Model results for a homogeneous viscoelastic model forced by a fortnightly tide. The values in the three panels match the description in figure 3.13. The average value of L_{tr} is 40.87±0.47 km.

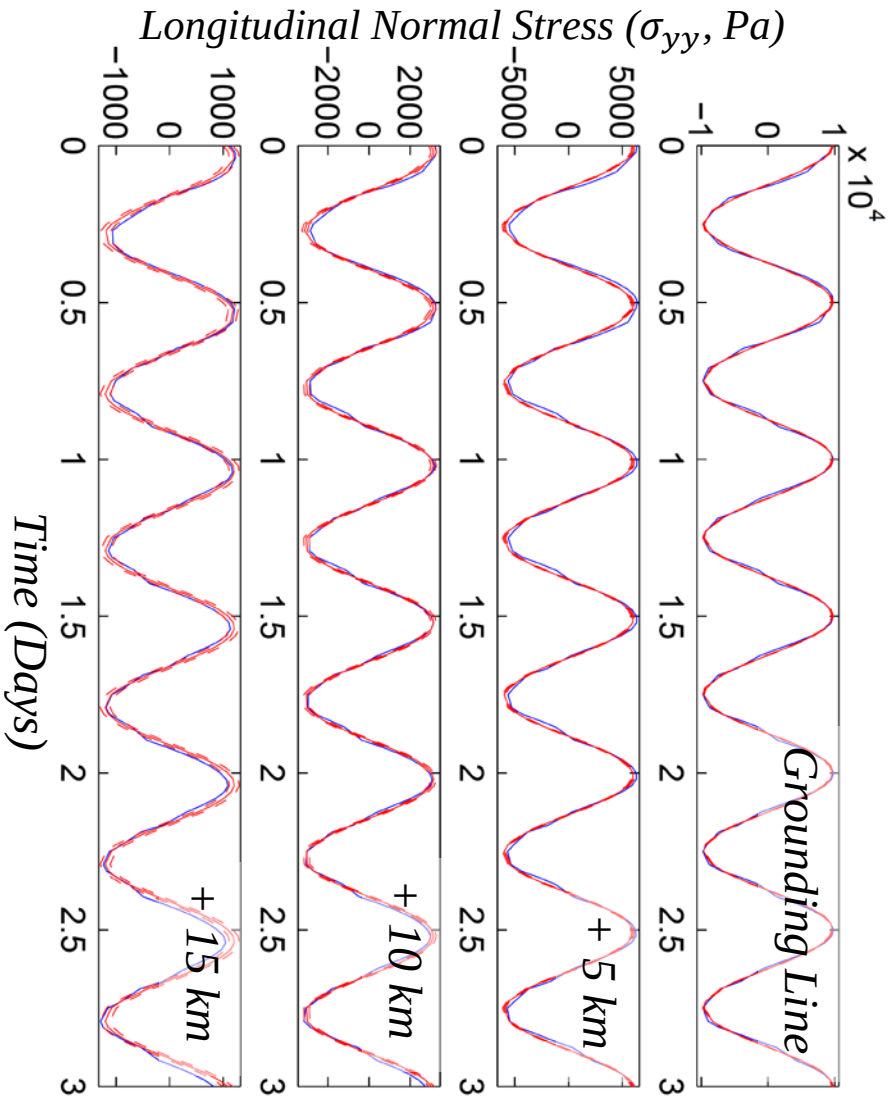

Figure 3.16: Model results and fits for locations on the model surface at the grounding line, and 5, 10, and 15 kilometers inland of the grounding line. The model has a homogeneous viscoelastic rheology and is forced with a semidiurnal tide. The blue lines are the model output, the solid red lines are the model fits using equation 3.15, and the dashed red lines are the 95% confidence intervals. The tidal stress diminished with distance inland of the grounding line, and the phase of the stress becomes increasingly delayed relative to the forcing frequency, which has a phase of zero degrees.

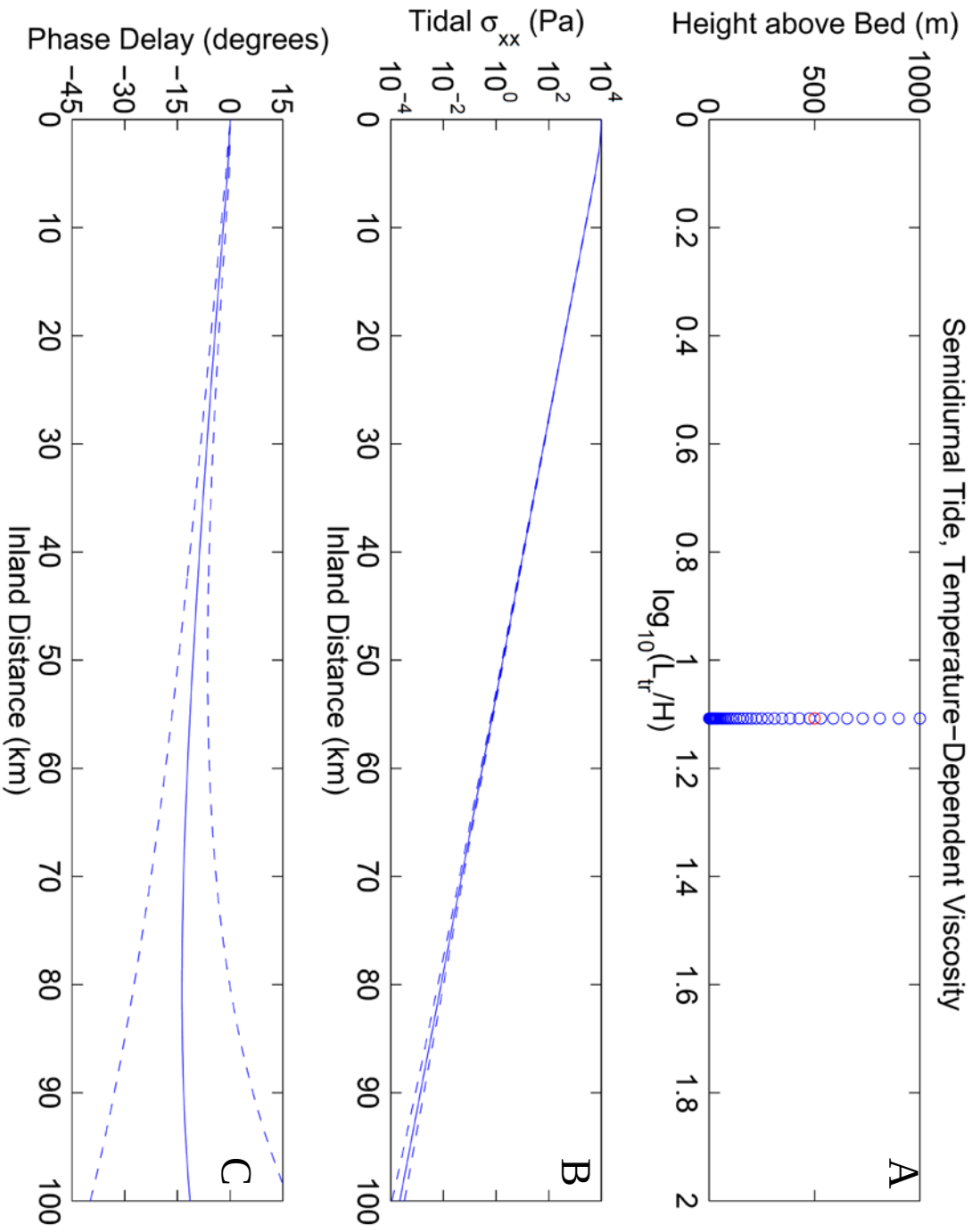

Figure 3.17: Model results for a temperature-dependent viscoelastic model forced by a semidiurnal tide. The values in the three panels match the description in figure 3.13. The average value of L_{tr} is 12.81±0.001 km.

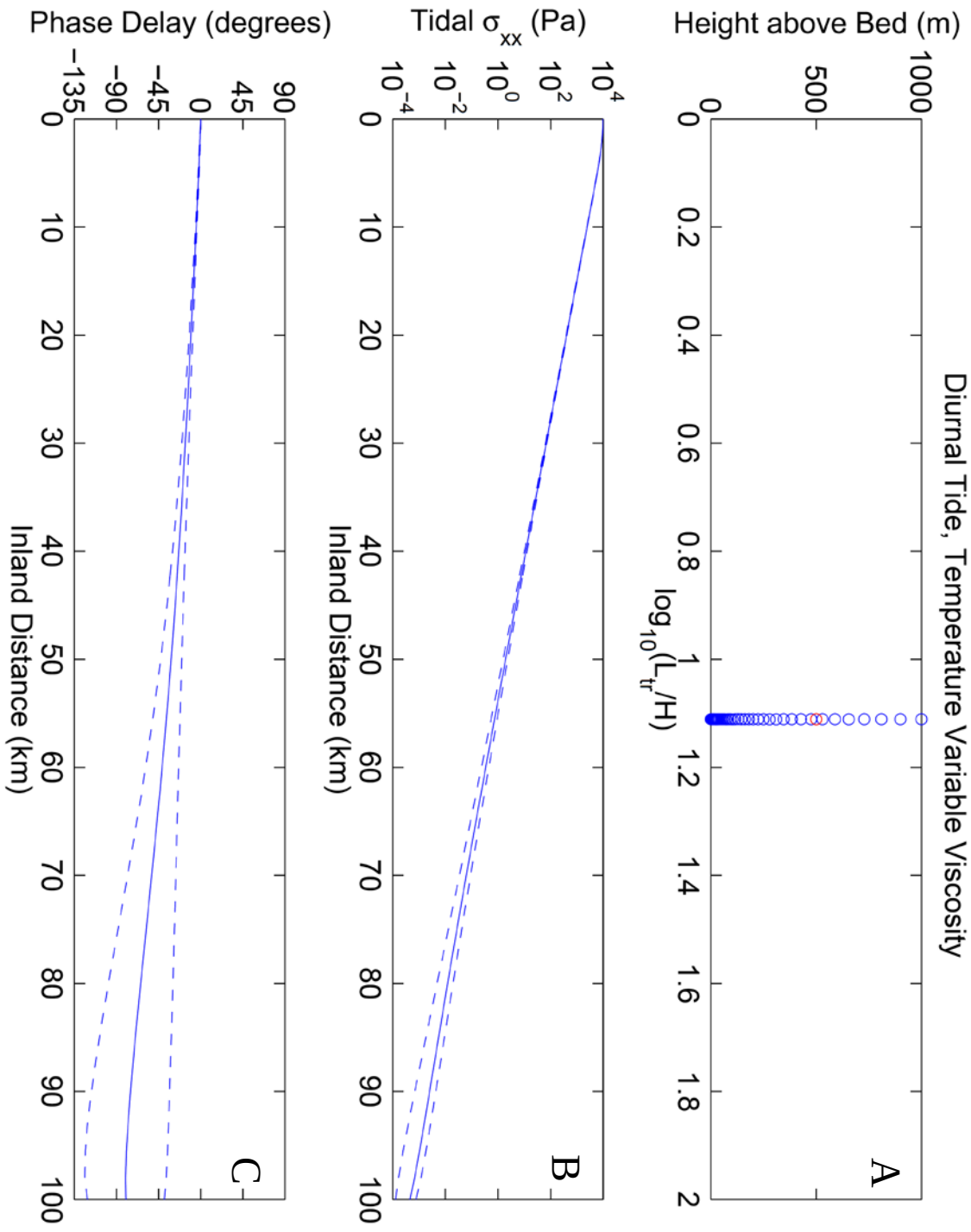

Figure 3.18: Model results for a temperature-dependent viscoelastic model forced by a diurnal tide. The values in the three panels match the description in figure 3.13. The average value of L_{tr} is 12.91±0.002 km.

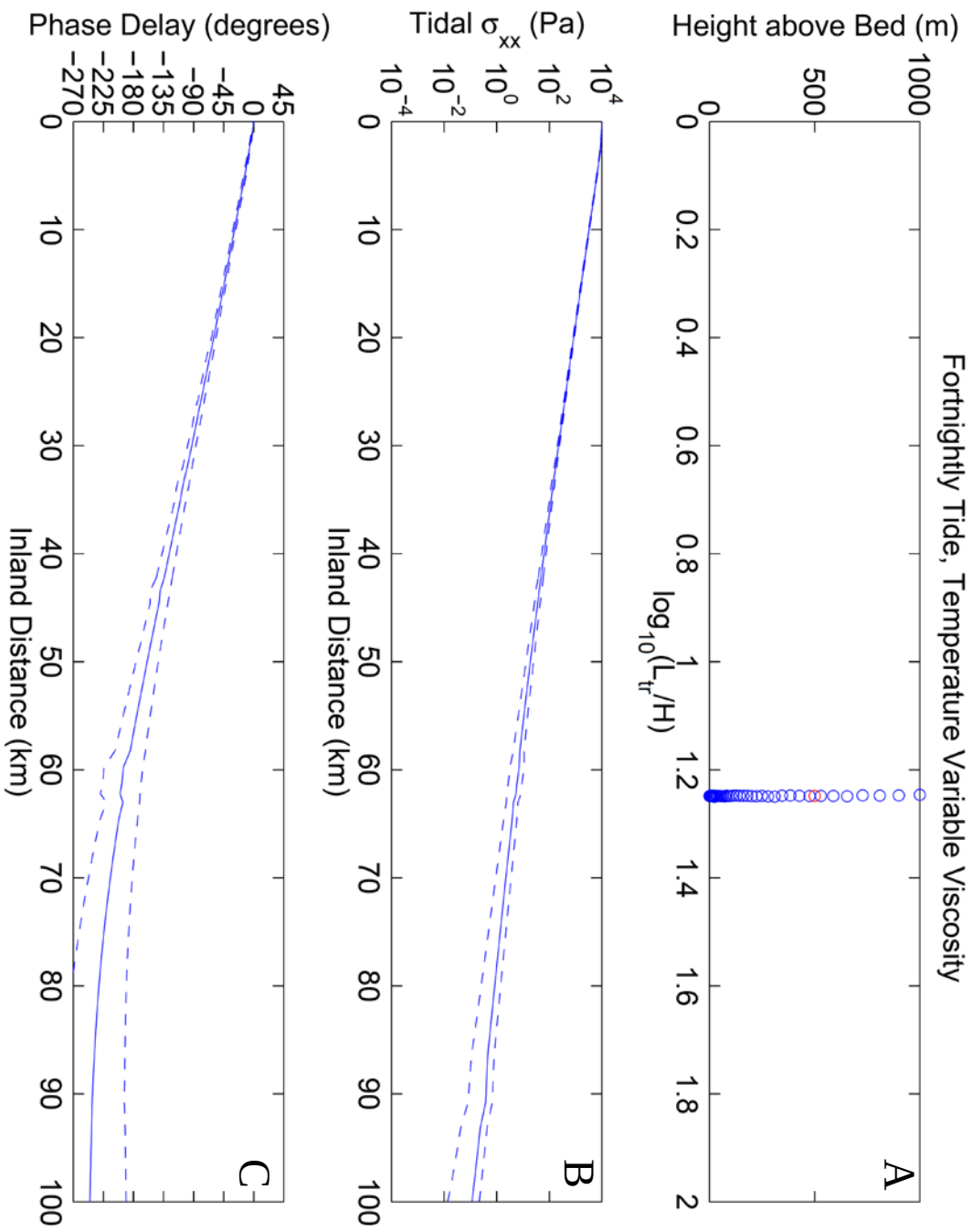

Figure 3.19: Model results for a temperature-dependent viscoelastic model forced by a fortnightly tide. The values in the three panels match the description in figure 3.13. The average value of L_{tr} is 17.72±0.03 km.

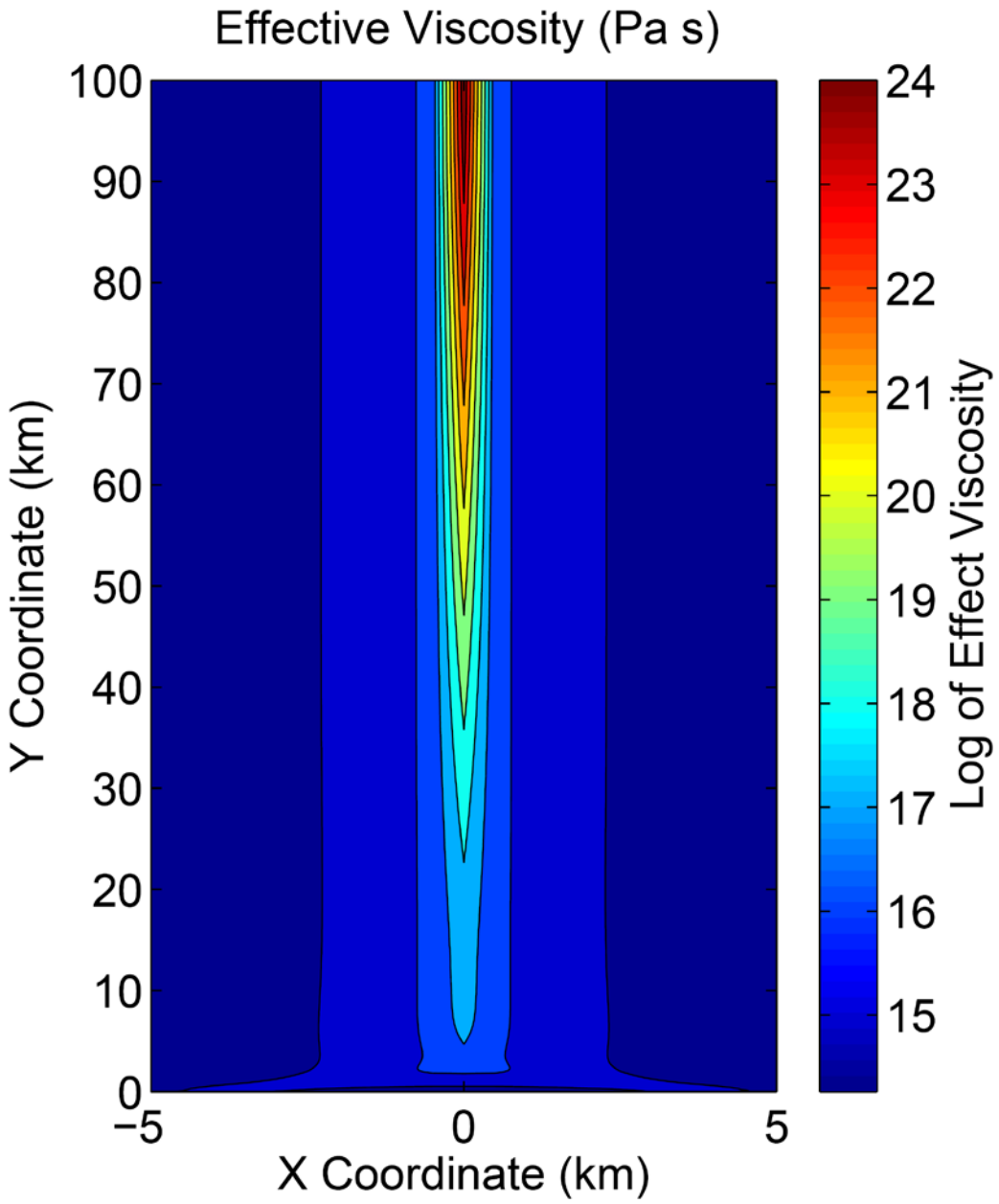

Figure 3.20: Figure showing the basal effective viscosity of our semidiurnal models for the homogeneous viscosity model. This figure demonstrates that the shear margins have substantially reduced viscosity relative to the central ice.

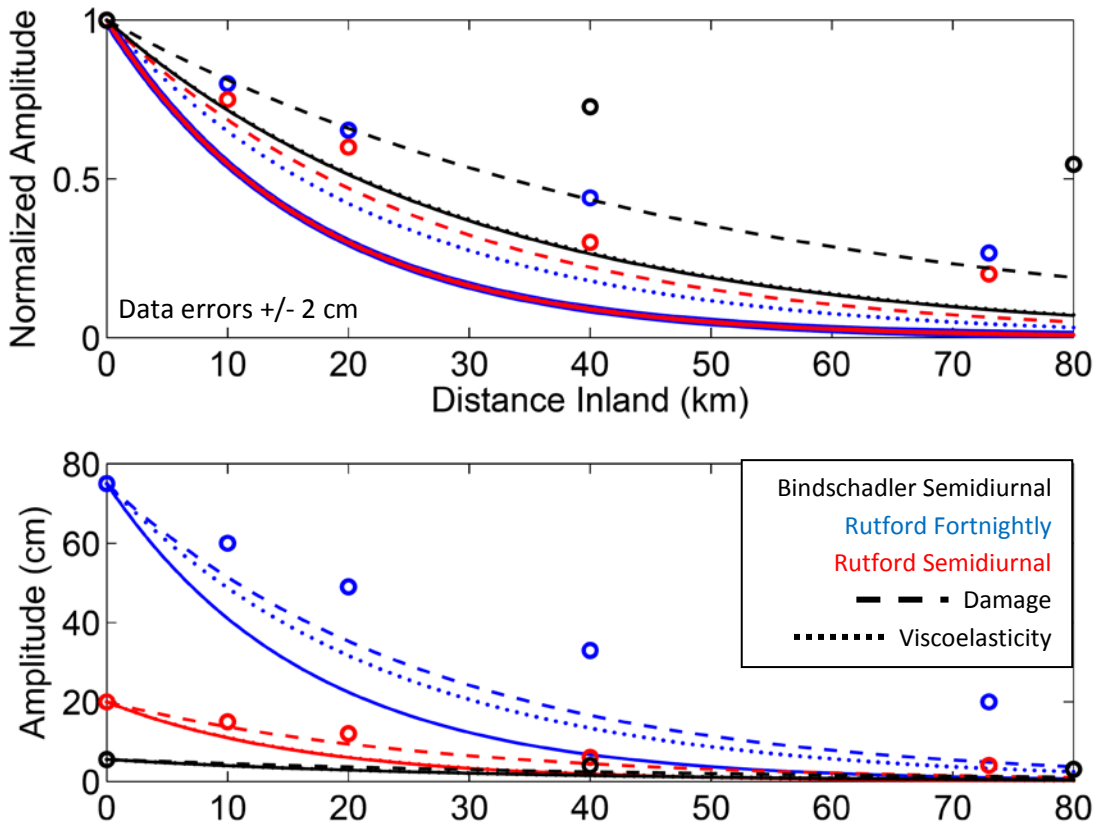

Figure 3.21: An updated version of figure 2.11 to reflect the added maximum effects of elastic damage in the shear margins (dashed) and temperature-dependent viscoelasticity (dotted). The solid line shows the linear elastic solution. The colors of the circles (data points) and lines refer to: blue, Rutford fortnightly tide; red, Rutford semidiurnal tide; black, Bindschadler semidiurnal tide. The upper panel shows the normalized amplitude of each tidal signal, while the lower panel shows the true amplitude.

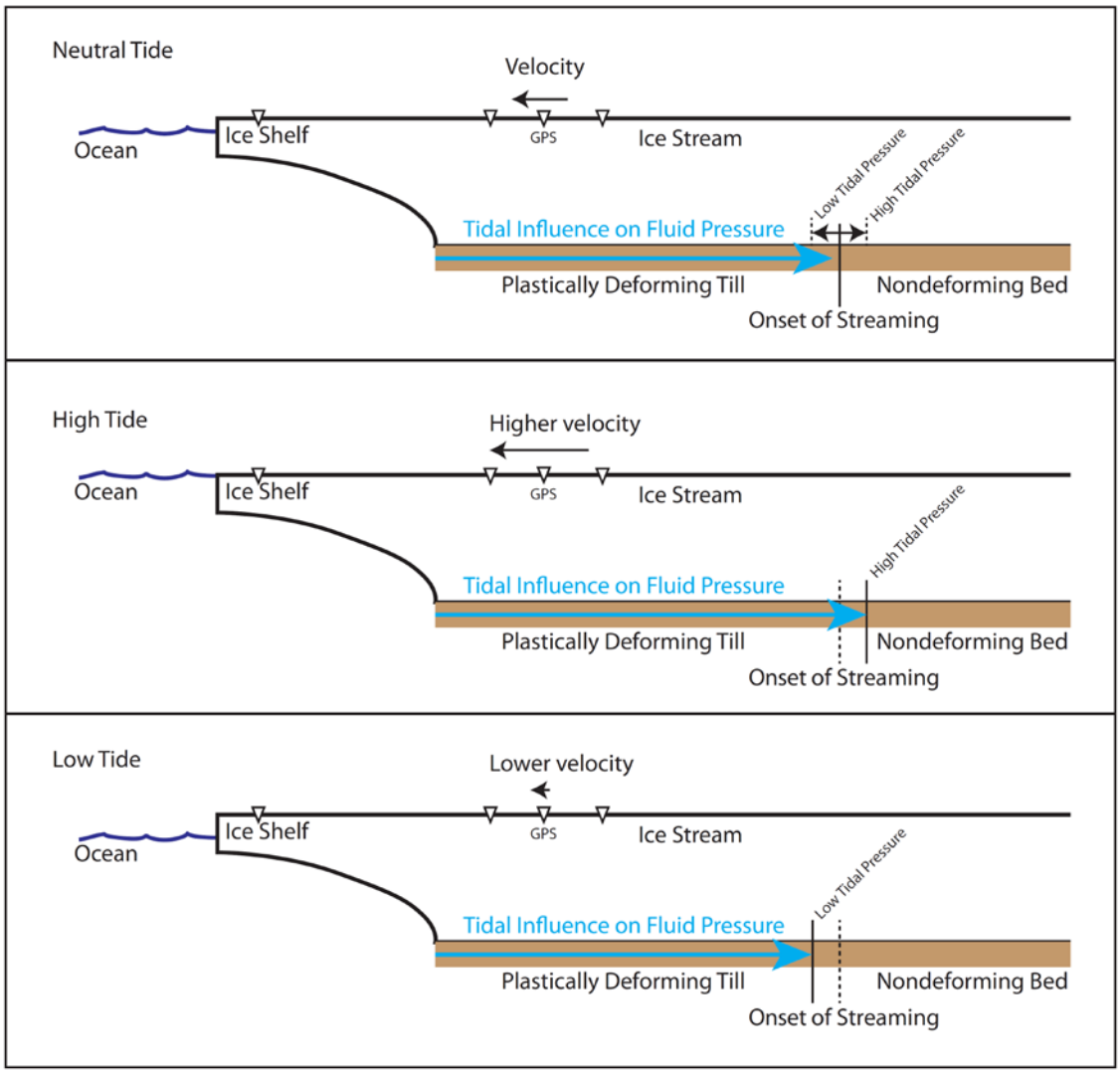

Figure 3.22: Schematic view of our hydrology hypothesis at a neutral, high, and low tidal amplitude, respectively. The triangles represent GPS stations on the surface of the ice stream and ice shelf. The brown layer represents the subglacial till. The onset of streaming is shown as a vertical line, and should vary in position with changes in the ocean tidal amplitude. Then the onset of streaming is farther inland, the GPS stations move faster relative to a neutral position as more of the ice is streaming. Furthermore, when the onset of streaming is closer to the grounding line, the relative velocity of the GPS stations is smaller than at a neutral tide.

Tidal Period	*E (GPa)*	0°C	-5°C	-10°C	-15°C	-20°C	-25°C
S	10	31.06	49.89	81.33	104.99	138.89	184.50
S	1	98.21	157.77	257.17	332.01	439.21	583.45
D	10	21.96	35.28	57.51	74.24	98.21	130.46
D	1	69.44	111.56	181.85	234.77	310.56	412.56
F	10	5.87	9.43	15.37	19.84	26.25	34.87
F	1	18.56	29.82	48.60	62.74	83.00	110.26

Table 3.1: Transitional stresses σ_{trans} for a range of ice temperatures, tidal frequencies, and Young's moduli. The transitional stress is defined in equation 3.7 and related discussion is in section 3.1.2.2. All values in table 3.1 are in *kPa*. The tidal period category uses the following abbreviations: S for semidiurnal, D for diurnal, and F for fortnightly.

	Semidiurnal				*Diurnal*				*Fortnightly*	
	M_2		S_2/N_2*		K_1		O_1		M_f	
	Amp	Phase	Amp	Phase	Amp	Phase	Amp	Phase	Amp	Phase
Weddell Data	1.52	35	0.843	339	0.620	11	0.497	57	0.0652	66
Weddell FES2004	1.30	59	0.886	92	0.419	62	0.405	56	0.0301	198
Ross Data	0.105	325	0.119	108	0.587	274	0.432	348	0.0286	5
Ross FES2004	0.012	30	0.028	352	0.367	316	0.261	295	0.0313	205

Table 3.2: Observational and tidal model amplitudes (in meters) and phases (in degrees) for the Weddell and Ross Seas. The flagged component of the semidiurnal tide is the only component that had a varying second-largest tidal component, with the S_2 being subdominant in the Weddell Sea while the N_2 being so in the Ross Sea. Note that the agreement between the tidal model and the floating ice data is not great (see text for discussion).

Tidal Period	Applied Force	Viscosity	L_{tr} (km)	c (m/s)
S	Full	Temp.	14.4	--
S	Simple	Temp.	12.8	1.8
S	Simple	Homog.	15.6	4.6
D	Full	Temp.	13.1	--
D	Simple	Temp.	12.9	1.7
D	Simple	Homog.	15.0	11.1
F	Simple	Temp.	17.7	0.94
F	Simple	Homog.	40.9	0.60

Table 3.3: Calculated values for the length-scale of stress-transmission in our viscoelastic models. The tide column describes the forcing frequency of the applied ocean load. The applied load defines the load as either the full tidal condition or the simple tidal condition (see Appendix 3A). The viscosity column defines if the given model for nonlinear viscosity used a temperature-dependent viscosity or a homogeneous viscosity coefficient. The values of L_{tr} are quoted in kilometers. The phase velocity, c, is the slope of the phase vs. distance plot, and is shown in units of m/s. Note that no phase velocity is calculated for the "full" tidal forcing functions. The tidal period category uses the following abbreviations: S for semidiurnal, D for diurnal, and F for fortnightly.

Appendix 3A: Full Tidal Loading vs. Partial Tidal Loading

Following the rationale of Cuffey and Paterson, 2011 (and references therein), the stress balance for an ice stream/shelf system would involve balancing the hydrostatic pressure at the edge of the ice shelf and that of the ocean. As the ice shelf is floating, there is a net "pull" on the ice stream due to the excess pressure in the ice shelf compared to that of the ocean. As our viscosity is stress dependent, to be strictly accurate, we need to account for this end stress in our models to accurately model the viscous deformation in the ice stream. However, as the problem is more numerically tractable with a simple oscillatory tidal condition based on our elastic loading condition, we compare the model output for these two tidal loads (called "full" and "simple," respectively). We find that having the more complex full tidal condition changes the length-scale for stress-transmission decay, L_R, by only about 20%, far below the factor of 3-4 change necessary to match observations. Thus, we use this as justification to use the more numerically favorable simple tidal condition.

3A.1 Full Tidal Loading Condition

In addition to the oscillatory load of the ocean tide, there are three major tidally-important stresses that a full tidal loading condition needs to consider. These stresses are incorporated into the balance of: the hydrostatic pressure of the flowing ice, the hydrostatic pressure of the static ocean water, and the flexural stress imposed on the grounding line due to the vertical motion of the ice shelf. Figure 3A.1 shows a schematic picture of the interaction of these stresses on an ice stream at neutral, high, and low tides.

First consider that the hydrostatic pressure of the ice and the water. For the ice, the value of the stress at a given depth is simply $\rho_I g(H_I - z)$. For the water, we first use

the flotation condition at the grounding line to find that the water rises to a height of $H_T = H_I\left(1 - {}^{\rho_I}/_{\rho_W}\right)$, which in turn leads to the definition of the hydrostatic pressure at levels where water exists as: $\rho_W g(H_T - z)$. However, this stress balance occurs at the edge of the ice shelf, not at the grounding line. We make use of the assumption that the ice shelf behaves elastically, which, following the results from our two-dimensional shelf models in chapter 4, allows us to move this stress balance to the grounding line without any decay of these stress values.

To account for the bending stress from ice flexure, we use the same simple beam theory presented in Appendix 2A of chapter 2. From this simple model for flexure, we expect that the flexural stress at the grounding line will be on the order of a few 100 *kPa* at a maximum (the exact value depends on the ice thickness and the geometry of the ice shelf).

The full load applied at the grounding line is the sum of these three stresses: the differential gravitational stress at the end of the ice stream, the flexural stress induced by the floating ice shelf, and the change in water weight due to the tide. Figure 3A.1 shows a graphical representation of these tidal loads, while equation 3A.1 shows the total form of this loading:

$$\sigma_{applied} = \begin{Bmatrix} -\rho_i g(H_i - z) & \text{if } z > H_t \\ -\rho_i g(H_i - z) + \rho_w g(H_t - z) & \text{if } z \leq H_t \end{Bmatrix} + F_{Tide}(t) * \left[\sigma_{flex}\Delta h\left(z - \frac{1}{2}H_i\right) + \rho_w g \Delta h\right] \quad (3A.1)$$

where H_i is the ice thickness, H_t is the water level relative to the base of the ice stream, $F_{Tide}(t)$ is a unit tidal forcing as a function of time, and σ_{flex} is the maximum amplitude of flexure for a unit tide. For a reasonable tidal loading, the maximum force comes from

the static "pull," which is on the order of 1 *MPa* at the base of a one-kilometer-thick ice stream, while the flexural stress is a few 1*00 kPas* and the tidal weight is a few *10 kPas*.

3A.2 Simple Tidal Loading Condition

For our simple loading condition, we apply the variable portion of the ocean tidal load as a normal traction to the grounding line. Mathematically, this condition is:

$$\sigma_{applied} = F_{Tide}(t) * \rho_w g \Delta h \qquad (3A.2)$$

This is identical to the approach taken in our linear elastic model, save that the applied stress is time-variable.

3A.3 Stress-transmission Comparison

Figure 3A.2 shows a comparison between the tidally induced σ_{yy} component of stress (as described in section 3.3.1) for a map view of the base of a model with our full (left) and simple (right) loading conditions taken at a peak in stress response. We first note that overall, the stress field is remarkably similar between the full and simple loading conditions. The only major difference occurs in the portion of the ice steam near the grounding line, where the full loading condition has elevated stress values than those of the simple loading model. Such an increase in the value of the stress near the grounding line in the full model is not surprising as the value of the applied load is larger in this model than with the simple loading condition.

However, beyond this point inland, the model stress states are nearly indistinguishable, suggesting strongly that neither the hydrostatic "pull" on the ice stream edge nor the flexural stress due to the ice shelf bending viscosity of the ice stream near the grounding line significantly enough to dramatically change the nature of the transmission of stress viscoelastically in the ice stream. Such results are keeping with the

earlier observation and model results suggesting that tidal flexure is a stress that is only seen locally to the grounding line. The similarity in the model results is reflected in the values of L_R calculated between these two models, which fall within 20% of one another (see table 3.3).

As the difference between model results in this case is only on the order of 20%, we feel safe in neglecting the full tidal loading condition for our purposes. In the current form of our problem, we are sensitive to changes in the value of L_R that amount to a factor of 3-4, and thus 20% is far below the threshold of usefulness to justify the increase complexity (and thus computation time) of our models with the full loading condition.

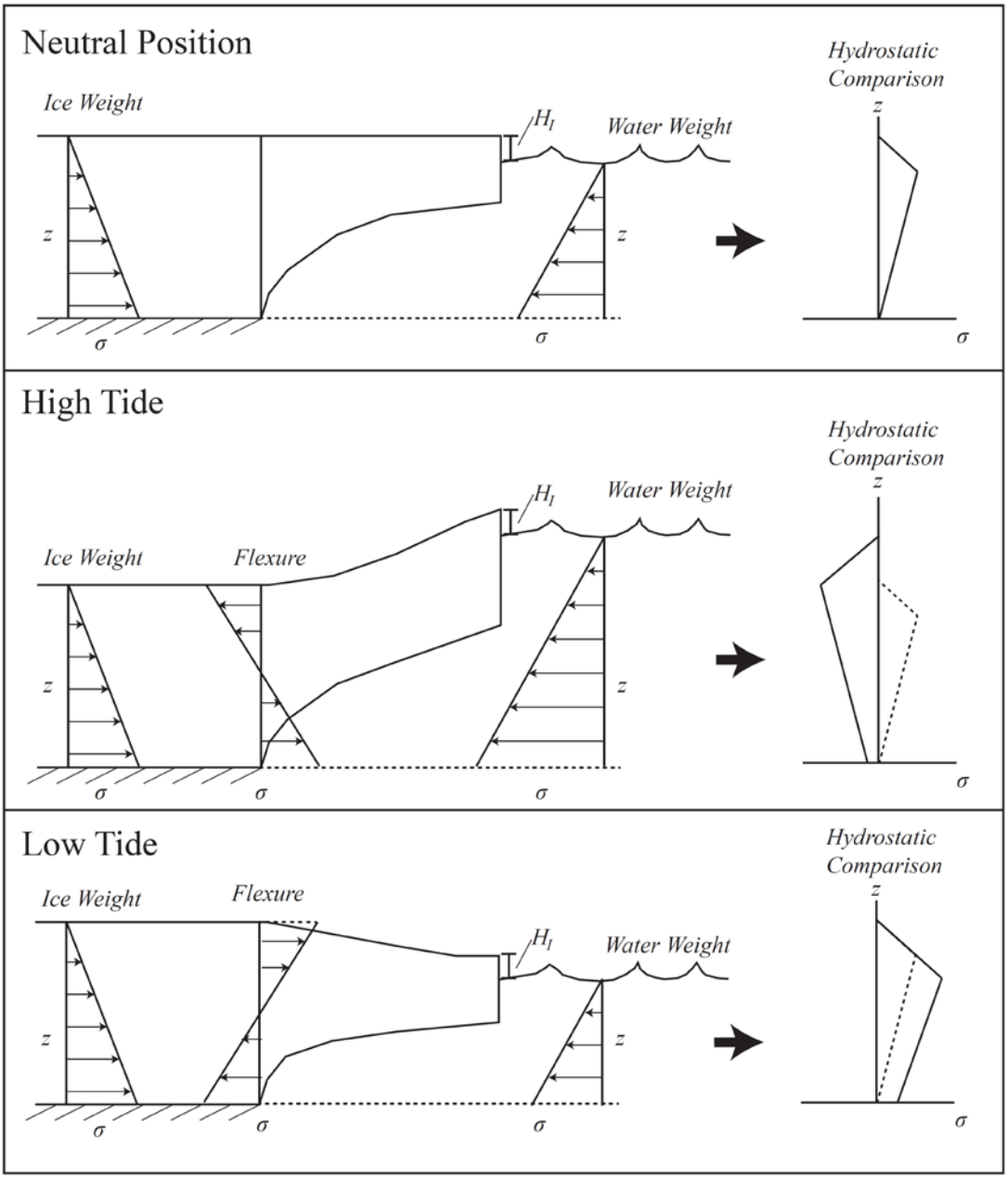

Figure 3A.1: Schematic diagrams of the full tidal forcing condition at a neutral, high, and low tide. The tidal stress will be the extensional/compressional stress due to the different in hydrostatic pressure at the edge of the ice shelf (shown in the graph on the right of the figure) and the flexural stresses due to the presence of the ice shelf. H_I is the distance between the surface of the ice shelf and the surface of the ocean.

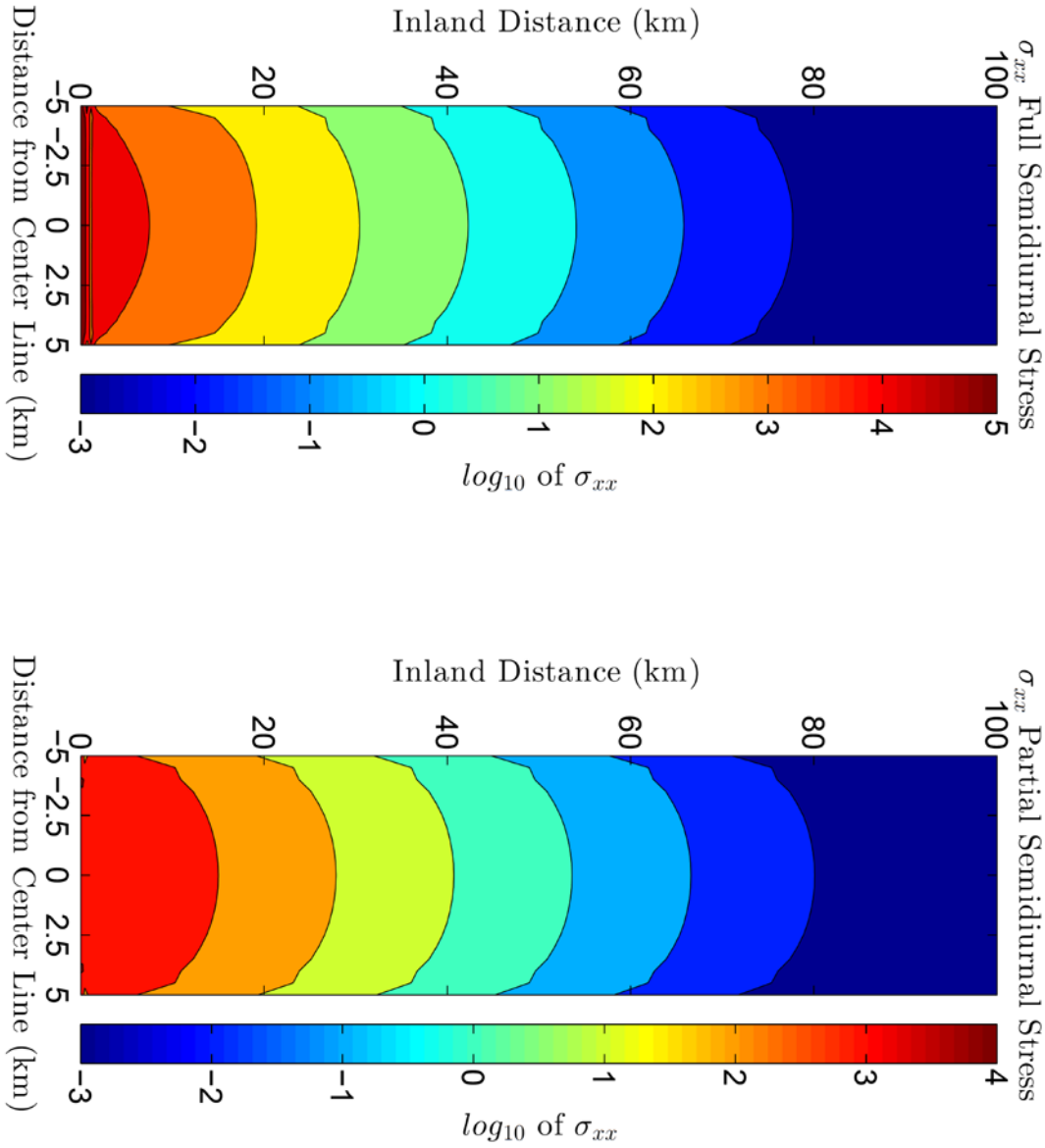

Figure 3A.2: Comparison of the value of the longitudinal normal stress (σ_{xx}) for the full tidal forcing condition (left) and the partial tidal forcing condition (right) at peak tidal amplitude. The full condition has a higher normal stress at the grounding line and a slightly more rapid decay of the stress due to the inclusion of the flexural stress. Once inland of the grounding line by five to ten kilometers, the stress-transmission length-scales are comparable between the two forcing conditions.